THESIS FOR THE DEGREE OF LICENTIATE OF TECHNOLOGY

Optical manipulation and heating of gold nanoparticles near interfaces

Daniel ANDRÉN

Department of Physics
Chalmers University of Technology
Göteborg, Sweden, 2018

OPTICAL MANIPULATION AND HEATING OF GOLD NANOPARTICLES NEAR INTERFACES

Daniel Andrén

Division of Bionanophotonics
Department of Physics
Chalmers University of Technology
SE-412 96 Göteborg
Sweden
Telephone: +46 (0)31 - 772 10 00

Cover:
(Left) Photograph of a sample during an experiment. Red laser light is focused by an objective to form optical tweezers for metallic nanoparticles. The prism guides green light for total internal reflection microscopy to determine nanoparticle-surface separation distance. (Right) Illustration of trapping and rotation of a metallic nanorod against a glass surface.

Printed in Sweden by
Chalmers Reproservice
Chalmers Tekniska Högskola
Göteborg, Sweden, 2018

CHALMERS UNIVERSITY OF TECHNOLOGY

Optical manipulation and heating of gold nanoparticles near interfaces

Daniel ANDRÉN

Department of Physics Licentiate of Technology

Abstract

By focusing laser light to small volumes, its momentum can be used to trap and manipulate objects in the size range from cells down to single atoms. Devices using this effect are called optical tweezers, and have found use in measuring and applying minuscule forces and torques, contributed to deepening our knowledge of molecular motors, unraveling the mechanics of cells and DNA, and better understand statistical mechanics and hydrodynamic interactions at the nanoscale. In short, the optical tweezer is a crucial component in our aspiration to understand and unlock the potential of nano-scaled objects.

One class of nano-elements worth devoting special attention to are nanoparticles supporting plasmonic resonances. These present strongly enhanced light-matter interactions and may find use in as diverse fields as high-density data storage, single molecule detection, and personalized medicine. One potential use of plasmonic nanorods is as rotary nanomotors. These are capable of reaching record rotation frequencies of several tens of kilohertz when optically trapped in water against a glass surface. This thesis focuses on studying vital questions related to such rotary nanomotors, which are interesting to resolve from both a fundamental and from an applied point of view.

It is well-known that metallic nanoparticles are efficiently heated by light. This will give rise to several photothermal effects affecting the nanoparticle and its surrounding. How these influence the performance of the nanomotor is evaluated. Through spectroscopic measurements, morphological changes induced by atomic migration is observed. Moreover, the elevated thermal environment around the nanoparticle is probed using two separate techniques, and temperatures above 200°C are routinely reached, but could be kept as low as a few degrees above ambient under the right circumstances.

The gold nanoparticle is trapped at a small, but hitherto unknown, distance from a glass interface. The vicinity to a surface can affect several of a nanoparticles properties, including its diffusion and thermal environment, and knowing this distance is hence critical for any claims about the nanomotors' performance. Therefore, total internal reflection microscopy is performed on the trapped nanoparticles and it is found that they are confined less than 100 nm from the surface. The distance can be controlled by altering the radiation pressure, or Coulomb repulsion.

In summary, the work performed in this thesis present important building blocks towards a complete understanding of this highly promising rotary motor system.

Keywords: optical tweezers, plasmonics, gold nanorod, nanomotor, photothermal effects, thermal reshaping, LSPR spectroscopy, Brownian dynamics, TIRM, particle-surface separation distance.

List of publications

The following papers are included in this thesis:

I **Probing Photothermal Effects on Optically Trapped Gold Nanorods by Simultaneous Plasmon Spectroscopy and Brownian Dynamics Analysis**
Daniel Andrén, Lei Shao, Nils Odebo Länk, Srdjan S. Aćmović, Peter Johansson, and Mikael Käll.
ACS Nano, 2018, 11, 10053 – 10061.

II **Construction and Operation of a Light-driven Gold Nanorod Rotary Motor System**
Daniel Andrén, Pawel Karpinski, and Mikael Käll.
Journal of Visualized Experiments: JoVE, 2018, 136.
`https://www.jove.com/video/57947/`

III **Surface Interactions of Gold Nanoparticles Optically Trapped Against an Interface**
Daniel Andrén, Nils Odebo Länk, Hana Jungová, Steven Jones, Peter Johansson, and Mikael Käll.
In manuscript

My contributions:

I: I performed all optical experiments and data analysis and wrote a draft of the paper.

II: I wrote a draft of the paper, and led the work on recording the video version of the article.

III: I performed optical experiments, Brownian motion simulations and data analysis and wrote a draft of the paper.

Papers not included in this thesis:

I **Gold Nanorod Rotary Motors Driven by Resonant Light Scattering**
Lei Shao, Zhong-Jian Yang, Daniel Andrén, Peter Johansson, and Mikael Käll.
ACS Nano, 2015, 9, 12542 – 12551.

II **Brownian Fluctuations of an Optically Rotated Nanorod**
Faegheh Hajizadeh, Lei Shao, Daniel Andrén, Peter Johansson, Halina Rubinsztein-Dunlop, and Mikael Käll.
Optica, 2017, 4, 746 – 751.

III **Photothermal Heating of Plasmonic Nano-antennas: Influence on Trapped Particle Dynamics and Colloid Distribution**
Steven Jones, Daniel Andrén, Pawel Karpinski, and Mikael Käll.
ACS Photonics, 2018, 5, 2878 – 2887.

IV **Photothermal DNA Release from Laser-tweezed Individual Gold Nanomotors Driven by Photon Angular Momentum**
Hana Šípová, Lei Shao, Nils Odebo Länk, Daniel Andrén, and Mikael Käll.
ACS Photonics, 2018, 5, 2168 – 2175.

V **Optically Controlled Stochastic Jumps of Individual Gold Nanorod Rotary Motors**
Lei Shao, Daniel Andrén, Steven Jones, Peter Johansson, and Mikael Käll.
Physical Review B, 2018, 98, 085404.

VI **Counter-Propagating Optical Trapping of Resonant Nanoparticles Using a Uniaxial Crystal**
Pawel Karpinski, Steven Jones, Daniel Andrén, and Mikael Käll.
Laser & Photonics Reviews, 2018, 12, 1800139.

VII **Large-Scale Fabrication of Shaped High Index Dielectric Nanoparticles on a Substrate and in Solution**
Ruggero Verre, Nils Odebo Länk, Daniel Andrén, Hana Šípová, and Mikael Käll.
Advanced Optical Materials, 2018, 6, 1701253.

Acknowledgements

The last two and a half years have for me been a great source of both personal growth and scientific advances. There are many people who have both inspired and helped me to get to this point, where I can present a licentiate thesis.

Firstly, my gratitude goes to my supervisor Mikael Käll. Thank you for believing in me, giving me the freedom to steer the project, and at the same time providing valuable guidance and suggestions. Your breadth of knowledge and ability to always ask the insightful questions are things that never cease to amaze me!

I will always be grateful to Lei Shao. Thank you, both for initially sparking my interest for nanoparticle rotation, and for everything you taught me regarding plasmonics, optical tweezers, and scientific methodology. I hope we will get the opportunity to work together again in the future!

A huge thanks to Steve Jones. You are inestimable, both as a friend and as a colleague. Performing my PhD studies side-by-side with you makes it both more enjoyable and easier!

Sincere thanks to Nils Odebo Länk. Neither this thesis, nor its constituent papers would have been possible without your continuous help and attention to detail. Not only are you an excellent researcher, you are also among the most easy-going and friendly people I know!

Ruggero Verre, I appreciate you teaching me nanofabrication. It has not come to much use yet in my own research endeavours, but I am certain I will have tremendous use for it moving forward and in my future career. Thank you for also being a bright and uplifting character, you can make the toughest problem seem like a walk in the park!

Another thanks goes to Hana Jungová, both for all the help with our shared research projects, but also for all of our discussions about life, academia and everything in between.

Also, a big thanks to the rest of the Bionanophotonics division, past and present group members, for making it a great place to work. You all know I have great things to say about you too. Unfortunately, my space here is limited. I hope that I am as much of a reason that you enjoy your job as you are that I enjoy mine!

Moreover, I am thankful to the Excellence Initiative Nano for believing in me and funding my research. I hope I will prove that I too am excellent!

Lastly, I would never have been able to finish this thesis without the constant support and encouragement from my lovely Carolina, and the rest of my family. Hopefully, you will all get to see me more after this is done!

Daniel Andrén
Göteborg, 2018/10/26

For Tra.

Because Tra is great!

Contents

Chapter 1

Introduction

When a high-intensity photoflash is put into close proximity to a cymbal and set off, the cymbal starts ringing. This has by many been put forth as a demonstration for the fact that light carries linear momentum that can affect matter. However, recent detailed investigations into the system show that the ringing is rather an effect arising from differential heating leading to a pulse of thermal expansion of the metal and that the transfer of photon momentum is quite negligible [1]. Nevertheless, transfer of photon momentum does occur to some extent. The overall effect was first suggested by Kepler in 1619 when observing comet tails pointing away from the sun, and predicted analytically by Maxwell in 1873. Despite the fact that the cymbal ringing is not solely an effect of photon momentum transfer, this experiment serves to illustrate two of the main components of this thesis. Namely, that light can strongly interact with matter causing both physical movement and heat generation, and many of the relevant physical phenomena can be discussed with this experiment as a starting point.

Let's suppose that you are wealthy and made the cymbal out of pure gold. It would be beautiful and shiny in the yellow metallic color we recognize. If you were to split it in half, its color and all other properties would remain unchanged. Continued division would lead to no further change; until we reach pieces of a few hundred nanometers, when the light-matter interaction of gold start showing a plethora of beautiful, interesting and highly tuneable effects [2, 3]. Depending on its exact size and dimension, the gold pieces will preferentially and very efficiently scatter light of specific colors, as seen in Figure 1.1. The gold in your cymbal has entered the realm of plasmonics, and its properties have been the focus of enthusiastic research efforts related to bio-sensing [4], medicine [5, 6], data storage [7], solar cells [8], photocatalysis [9], and flat optical components [10] to name a few. In this thesis, gold nanoparticles are studied and as a background to their light-matter interactions the field of plasmonics is introduced in Chapter 2.

If one changes the photoflash to a continuous laser source, and illuminate a nanoscopic piece of gold with light that has been focused through a strong lens, the previously negligible photon momentum will affect the nanoparticle with a significant force. If the laser's intensity is sufficient, this force will even have the ability to immobilize the object. This was essentially the revelation that Arthur Ashkin made when performing similar experiments on μm-sized latex beads [11], and subsequent

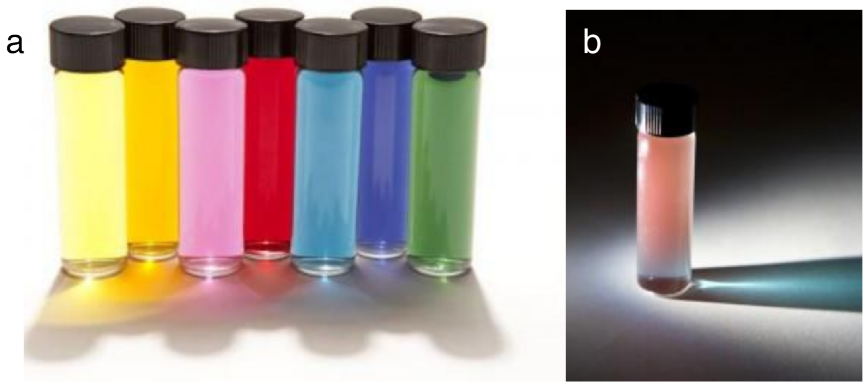

FIGURE 1.1: (a) Gold and silver nanoparticles of different sizes and shapes. The colloidal solutions contain (from left to right): Silver nanospheres (80 nm), silver nanospheres (20 nm), gold nanospheres (40 nm), gold nanospheres (12 nm), silver nanoplates (200 nm), silver nanoplates (120 nm), silver nanoplates (60 nm). (b) Incoming white light on gold nanoparticles that absorb and scatter green and red light, so that the light transmitted is blue. Image from nanoComposix, a company which markets colloidal nanoparticles.

experiments led to the development of the "single-beam gradient optical trap" [12, 13]. These so-called optical tweezers have produced ripples through both the academic as well as industrial landscape, with proven usefulness in as diverse fields as molecular biology for studying forces [14–16], and for cooling single atoms in atomic physics [17, 18]. Its usefulness is well illustrated by the 2018 Nobel prize being awarded to Ashkin for the conception of optical tweezers.

When attempting to trap metallic nanoparticles, it first seemed their strong light-matter interactions, and particularly scattering, rendered them impossible to confine in three dimensions. Yet, in 1994, it was realized that if the trapping laser wavelength was far from the absorption peak of the nanoparticle, the attractive force from the focused laser overcame the destabilizing scattering and three dimensional confinement, even more stable than for similarly sized dielectric particles, was possible [19]. Since then, three-dimensional optical trapping of metallic nanoparticles has been studied in detail from the fundamental perspective [20–24], and produced a range of interesting possible applications, within thermal generation and thermodynamics [25–28], as well as novel nanofabrication techniques [29], the study of biological systems [30, 31], and enhanced chemical reactions [32], to name a few. The optical tweezers background that is fundamental to the work performed in this thesis is presented in Chapter 3.

Not only can light affect matter via momentum, it turns out that angular momentum can be transferred to an object under the right circumstances [33]. Hence, if the light from the photoflash striking the cymbal was circularly polarized and intense enough, the cymbal would twist as well as ring as the flash goes off! Just as the momentum transfer is negligible at macroscopic scale, so is transfer of angular momentum. Yet again, as the size of the cymbal piece decreases also the applied optical torque becomes noticeable. As with optical tweezing, the initial studies of optically induced torque were performed on dielectric microparticles [34–36]. Just

as in the overarching field of optical tweezers, it was soon realized that the plasmonic properties of metallic nanoparticles made them relevant for optical rotation schemes as well [37, 38]. Unfortunately, the metallic nanoparticles that produce the most torque are the least optimal for 3D trapping. The large scattering of such nanoparticles leads to the particle being pushed rather than immobilized by the light. To mend this problem, a surface with the same charge polarity as the nanoparticle was used as a barrier, whereby the pushing force was counteracted by Coulomb repulsion from the surface. In this approximately two-dimensional geometry, nanoparticles could be stably trapped and exceptionally high rotation rates could be achieved [39, 40]. Initial tests indicated promise of these rotary nanomotors as a tool for nano-rheology and molecular sensing. An overview of the background of this rotary motor system as well as a summary of other techniques used is given in Chapter 4.

The cymbal heated up when the photoflash hit it, eventually causing the ringing sound, and light-induced thermal effects are pronounced for materials on all size scales. For plasmonic particle the heating is highly pronounced due to the strongly enhanced light-matter interactions from the resonance effect. This heating can be detrimental in some applications, particularly temperature-sensitive biological experiments; however, it can also be advantageous in the field of thermoplasmonics [41], spurring research fields such as photothermal imaging [42], plasmonic photothermal therapy [43], and nanosurgery [44]. In Paper I, we evaluate the photothermal effects related to the operation of the nanomotor and observe nanoscale thermal gradients as well as photothermally induced morphological changes of the nanoparticles. Moreover, in order to display the ease of operation and versatility of this rotary motor system, a detailed outline of the construction and operation of the system is presented in a method-paper (Paper II).

Throughout previous studies, the separation distance between the trapped nano-particle and the repulsive surface has remained unknown. Particle-surface interactions can give rise to alterations in hydrodynamic properties, Brownian motion, optical, as well as thermal properties of the trapped object. Hence, knowledge of the separation distance is critical for making any confident claims based on the technique. Therefore, in Paper III, analysis and measurements are performed to characterize nanoparticle/surface interaction and separation distance. The results are thereafter discussed in the context of the nanomotor platform studied.

Chapter 5 presents the experimental details needed to reach the results of the appended papers. Since the details necessary for Paper I are thoroughly laid out in the method-paper (Paper II), these are only summarized briefly. Rather, Chapter 5 mainly focuses on the details specific to the work done in Paper III.

To conclude this thesis, in Chapter 6 the main findings in the appended papers are summarized. Moreover, an outlook is provided to address unresolved issues as well as to outline possible future applications of gold nanoparticle trapping experiments.

Chapter 2

Plasmonics

Nanotechnology deals with structures where at least one dimension is reduced to the nanoscale. This results in drastic alterations to the electronic properties, such as the density of states and the electronic motion, since surface effects will now play an essential role. In the field of plasmonics, one analyzes how electromagnetic fields can interact with, and be confined within nanostructured matter, i.e. on length scales smaller than the wavelength of light. It turns out that the electronic structure of noble metals lends itself excellently to form nanostructures which strongly enhance light-matter interactions. If all three dimensions of a noble metal structure are reduced to the nanoscale, this nanoparticle will support an effect known as localized surface plasmon resonance (LSPR). As this resonance occurs, the nanoparticle's scattering and absorption will be significantly enhanced at specific wavelengths. For gold and silver nanoparticles this enhancement occurs in the visible part of the electromagnetic spectrum.

The field of plasmonics has become well established over the course of the last few decades, and the frontiers for both understanding and applications are still moving forward rapidly. Hence, the theory presented in the following chapter should be seen as a summary of the fundamental concepts rather than in-depth derivations of the formulas. Curious readers, or students new to the field, are directed to the following textbooks [2, 3], or reviews on the topics [45–47].

2.1 Drude model

The linear optical properties of a material can be described by its dielectric function $\varepsilon(\omega)$, which is a complex-valued and frequency dependent property. Materials with a negligible absorption have strictly real dielectric functions that tend to be nearly constant at optical frequencies, which is why it is often referred to as the dielectric constant or permittivity. In the case of metals, the dielectric function has a negative real part and a non-zero imaginary component, which both have strong frequency dependences and endows metals with a rich optical response.

A simple approximation for the dielectric function of a material is found by considering the conduction electrons as a free electron gas driven by an incoming electric field E. This approach was developed by Drude in 1900 [48] and is now referred to as the Drude model. The equation of motion for

the electrons in one dimension can be written as a driven, damped harmonic oscillator as

$$m_e\ddot{x}(t) + m_e\zeta\dot{x}(t) = -eE(x,t), \tag{2.1}$$

where m_e is the electron mass, and e its charge. $\zeta = \frac{1}{\tau}$ is the characteristic damping frequency, and τ the carrier relaxation time. By performing a Fourier transform in terms of angular frequency ω, one can after some reorganization reach an expression for the polarization density as

$$P(\omega) = -\frac{ne^2/m_e}{\omega^2 + \mathrm{i}\zeta\omega}E(\omega), \tag{2.2}$$

with n being the number of electrons per unit volume. Assuming a homogeneous and isotropic material, the polarization $P(\omega) = \varepsilon_0(\varepsilon(\omega) - 1)E(\omega)$, and the Drude model's expression for the dielectric function can be written as

$$\varepsilon(\omega) = 1 - \frac{ne^2/m_e\varepsilon_0}{\omega^2 + \mathrm{i}\zeta\omega} = 1 - \frac{\omega_p^2}{\omega^2 + \mathrm{i}\zeta\omega}\ , \tag{2.3}$$

where $\omega_p = \sqrt{ne^2/m_e\varepsilon_0}$ is the plasma frequency. The first term in Eq. (2.3) is for the ideal case of a free electron gas. To correct for the contribution of positive ion cores, this term can be replaced by a high-frequency limit correction term, ε_∞ [49]. The overall shape of the dielectric function of metals and hence its optical response is well captured by this simple approximation, as seen in Figure 2.1. Yet for gold, it does not predict the optically induced transitions between the valence and conduction band (often referred to as interband or d-band transitions), which enhance absorption below a wavelength of 600 nm. The discrepancy is seen most clearly for Im$\{\varepsilon\}$ in Figure 2.1b.

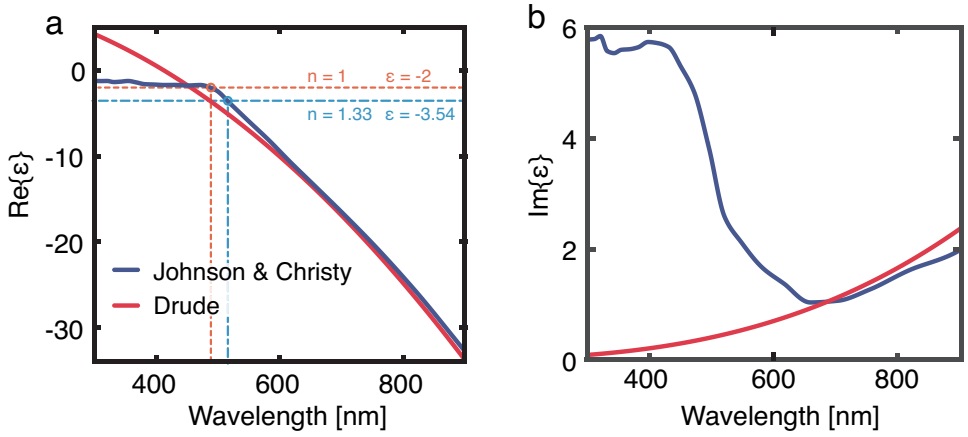

FIGURE 2.1: Real (a) and imaginary (b) part of the dielectric function for gold from the Drude model, calculated for an electron density of $5.9 \cdot 10^{28}\mathrm{m}^{-3}$, $\varepsilon_\infty = 9$, and carrier relaxation time of $\tau = 27.3$ fs [50], compared to the one experimentally measured by Johnson and Christy [51]. In particular, note the good agreement in the visible red and NIR spectrum, and the discrepancy that becomes apparent at shorter wavelengths, especially for Im$\{\varepsilon\}$ due to interband transitions in the metal.

2.2 Localized surface plasmon resonance

A plasmon is the collective oscillation of the conduction electrons in a material, excited by an electromagnetic field. The oscillation will be resonantly driven when the frequency of the incoming electromagnetic field matches a condition set by the material's properties, its shape, and surroundings. Plasmons come in three different forms, with the first and simplest one being the bulk plasmons, which is the collective conduction electron oscillation in the bulk of a metal. If a thin layer of a plasmonically responsive material is placed on a substrate of positive permittivity the conduction electrons in the metallic film can be resonantly excited by an electric field, and the second type of plasmon is induced, a surface plasmon resonance (SPR). Such oscillations are indeed interesting, and in fact, the most studied and commercialized type of plasmonic effect [2, 52, 53]. However, they are not further discussed in this thesis. The third type of plasmon resonance and the one we direct our attention to below is the *localized* surface plasmon resonance (LSPR), which occurs when all three dimensions are on the nanoscale.

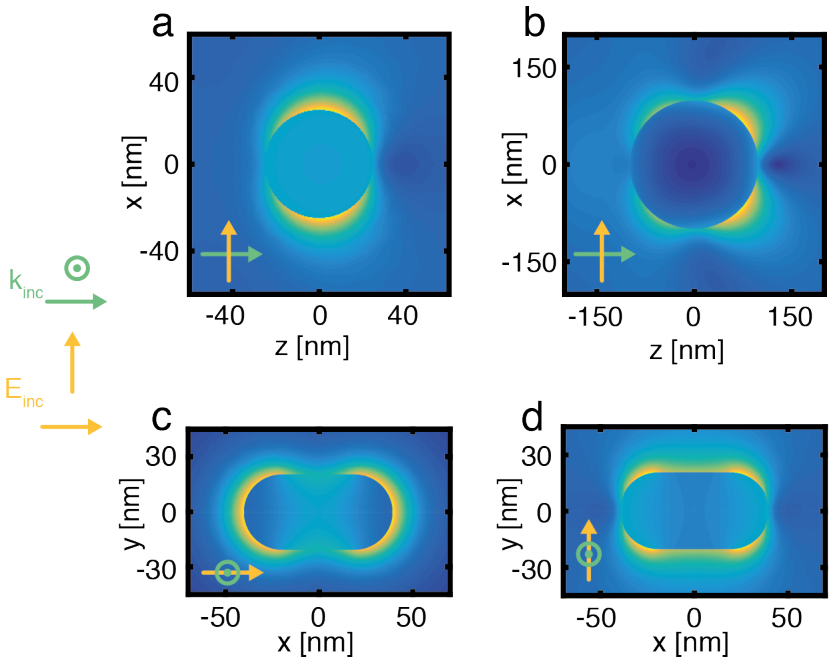

FIGURE 2.2: Electric field magnitudes for different particles excited by plane waves. The electric fields are normalized to their maximum values. Green arrows indicate the direction of the plane wave, and yellow line the direction of polarization. The conduction electrons are affected by the electric field and start oscillating. When the frequency of the field matches the LSPR frequency, a collective electron oscillation is induced. (a) Field for a spherical particle of $r = 25$ nm excited at $\lambda = 525$ nm, where the dipolar mode dominates. (b) Field for a spherical particle of $r = 100$ nm excited at $\lambda = 560$ nm, where the quadrupolar mode is dominant. (c) and (d) show electric fields around a nanorod of dimensions 40x80 nm for light polarized along the longitudinal (d, $\lambda = 612$ nm) and transverse (e, $\lambda = 525$ nm) direction.

The localized surface plasmon resonance behaviour is strongly dependent on the shape of the resonant particle. For a small nanosphere, only a dipolar resonance is excited (Figure 2.2a), whereas larger nanospheres can support

higher order modes, e.g. quadrupolar as in the one seen in Figure 2.2b[1]. For anisotropic nanoparticles, such as nanorods, the single spherical resonance is split into two separate resonance modes. These modes are corresponding to resonant excitations of the free electrons in the longitudinal or transverse direction of the rod (Figure 2.2c,d).

When the resonance condition is fulfilled, the scattering and absorption cross sections of a nanoparticle at this wavelength of light are strongly enhanced. Properties such as resonance wavelength, mode of oscillation, and damping characteristics, can be further varied widely depending on other particle properties such as size, material, and the properties of its surrounding.

2.2.1 Quasi-static approximation

The resonant behavior of the particle can to a first approximation be described, for a particle that is considerably smaller than the wavelength of the incident light ($d \ll \lambda$), with the so-called *quasi-static approximation*. Here, the optical response of the particle is described solely by its induced dipole moment and any spatial variations of the field within the nanoparticle are neglected. Such approximations can be regarded as accurate for nanostructures with dimensions below $30\,\mathrm{nm}$. It is possible to expand the model to include slightly larger particles ($< 100\,\mathrm{nm}$), if retardation effects from radiative damping as the particle's size increases and size-induced depolarization from emission at different points in the particle is taken into account. These retardation effects are captured in the modified long wavelength approximation (MLWA) [54, 55].

The analytical framework within the quasi-static approximation shows good agreement with experimental results for small spheres and spheroid-like particles, but it deteriorates for larger particles. However, with a slightly more involved approach, it is still possible to analytically calculate the optical response of an arbitrary sphere. By solving Maxwell's equations in spherical coordinates one can obtain converging infinite series of multipoles that describe the electromagnetic field at any point. This was found by Gustav Mie in 1908 [56] and is now referred to as Mie theory [57].

For particles or collections of particles with more complex shape and less symmetry, no analytical solutions are known and the community instead relies on numerical simulations to estimate their optical response. Such numerical methods are numerous, and grid-based approaches like finite difference time domain (FDTD), discrete dipole approximation (DDA), finite element methods (FEM), and boundary element methods (BEM) allow for simulation of any arbitrary geometry. They rely on being able to divide the nanoparticle into small domains and solving Maxwell's equations numerically in the time or frequency domain [58].

[1] The asymmetry in the electric field distribution stems from retardation effects, which are not captured in the quasi-static approximation discussed in Section 2.2.1.

Spherical case

The simplest case to consider is a small isotropic homogeneous sphere of radius r_0 with the dielectric function $\varepsilon(\omega)$ that is located in an isotropic and non-absorbing medium with the dielectric constant ε_m. By solving the Laplace equation for the electrostatic case and applying appropriate boundary conditions (details outlined in [2]) the induced dipole moment by a driving electric field $\mathbf{E}$ for the sphere is found to be

$$\mathbf{p} = 4\pi\varepsilon_0\varepsilon_\mathrm{m} r_0^3 \frac{\varepsilon(\omega) - \varepsilon_\mathrm{m}}{\varepsilon(\omega) + 2\varepsilon_\mathrm{m}} \mathbf{E} = \varepsilon_0\varepsilon_\mathrm{m}\alpha(\omega)\mathbf{E}, \tag{2.4}$$

where $\alpha = 4\pi r_0^3 \frac{\varepsilon(\omega)-\varepsilon_\mathrm{m}}{\varepsilon(\omega)+2\varepsilon_\mathrm{m}}$ is defined as the polarizability of the sphere. From the shape of $\alpha(\omega)$ it is realized that a resonant enhancement occurs as $\varepsilon(\omega) \to -2\varepsilon_\mathrm{m}$ for a certain ω, i.e. where the real part of the dielectric function of the metal equals -2 times the dielectric constant of the environment.

Already at this point, one of the most valuable properties of LSP resonances can be discerned. Since the dielectric function of metals has a strong dispersion in the visible spectrum, the LSPR resonance position becomes very sensitive to the surrounding dielectric environment[2] (ε_m). Since $\mathrm{Re}\{\varepsilon(\omega)\}$ is a decreasing function, the LSP resonance will redshift as the refractive index of the surrounding increases. This is illustrated in Figure 2.1a by the two lines marking ε_m for air and water, respectively. To use the sensitivity to refractive index shifts as a sensor is one of the most investigated properties of LSP resonant particles [46].

Spheroidal case

Maybe the most common type of nanoparticle that is studied in plasmonics nowadays is the nanorod. They are usually hemispherically capped cylinders, or capsule shaped. To enable analytical calculation within the quasi-static approximation, the capsule shape is approximated as a prolate spheroid with semi-major axis a and semi-minor axis b. Expressions for polarizabilities on the same form as Eq. (2.4) for each separate axis (j) of the spheroid, representing the longitudinal and transverse resonance modes are then found as

$$\alpha_\mathrm{j}(\omega) = \frac{4\pi ab^2}{3P_\mathrm{j}} \frac{\varepsilon - \varepsilon_\mathrm{m}}{\varepsilon + \left(\frac{1-P_\mathrm{j}}{P_\mathrm{j}}\right)\varepsilon_\mathrm{m}}, \quad \mathrm{j} = \mathrm{L\ or\ T}, \tag{2.5}$$

where P_L and P_T are depolarization factors for the longitudinal as well as transverse direction of the spheroid [57]. These are expressed in terms of the eccentricity $e = \sqrt{1 - \left(\frac{b}{a}\right)^2}$ by

[2] At optical frequencies, where the magnetic response (i.e. permeability) is insignificant, the refractive index of the environment relates to the dielectric constant as $\varepsilon_\mathrm{m} = n_\mathrm{m}^2$. Hence the statement that the LSP resonance is sensitive to the refractive index of the surrounding media.

$$P_{\mathrm{L}} = \frac{1-e^2}{e^2}\left[\frac{1}{2e}\ln\left(\frac{1+e}{1-e}\right)-1\right], \qquad (2.6) \qquad P_{\mathrm{T}} = \frac{1-P_{\mathrm{L}}}{2}. \qquad (2.7)$$

For anisotropic particles, it is useful to construct a three-dimensional matrix containing the polarizabilities of the three separate axes. As the axes of the spheroid are aligned with the Cartesian coordinate axes, the matrix that is often referred to as the polarizability tensor will be diagonal. The polarizability tensor can further be decomposed into a real and imaginary part according to $\boldsymbol{\alpha} = \boldsymbol{\alpha}' + \mathrm{i}\cdot\boldsymbol{\alpha}''$.

Optical cross sections

Under the quasi-static approximation, the experimentally determinable and useful properties of scattering and extinction cross sections for a particle can be derived as the corresponding properties for a point dipole as

$$\sigma_{\mathrm{scat}} = \frac{k^4}{6\pi}\left|\alpha(\omega)\right|^2, \qquad (2.8) \qquad \sigma_{\mathrm{ext}} = k\mathrm{Im}\{\alpha(\omega)\}, \qquad (2.9)$$

where $k = \frac{\omega n_{\mathrm{m}}}{c}$, and n_{m} is the refractive index of the medium, and c the speed of light in vacuum [2]. From these two equations, one can also calculate the absorption cross section as $\sigma_{\mathrm{abs}} = \sigma_{\mathrm{ext}} - \sigma_{\mathrm{scat}}$. Interestingly, around the LSP resonance the optical cross section for a nanoparticle can be much larger than its physical area, again demonstrating its strong interaction with light.

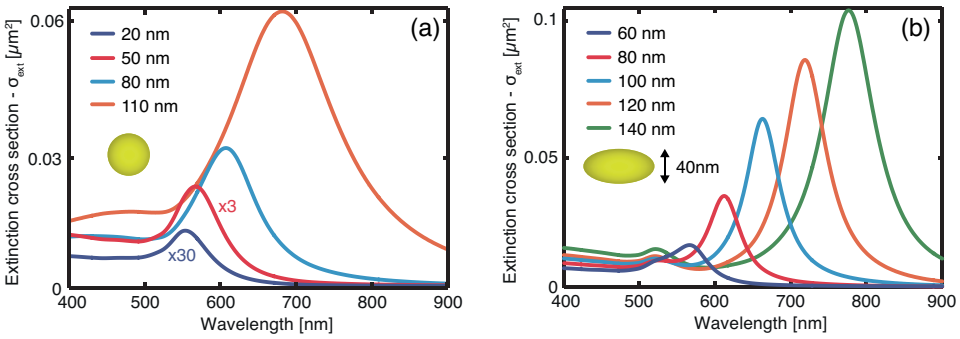

FIGURE 2.3: Extinction cross section spectra calculated for unpolarized light within the quasi-static approximation with applied MLWA corrections for (a) spherical gold particles with increasing diameter, and (b) spheroidal gold nanorods with a fixed width (40 nm) and increasing length.

Using the dielectric function for gold experimentally measured by Johnson and Christy [51], the extinction cross section in the quasi-static approximation for gold spheres of increasing diameter (Figure 2.3a) and gold rods of fixed diameter and increasing length (Figure 2.3b) can be calculated under MLWA correction. For the sphere case, the LSPR peak position is seen to redshift and broaden as the particle size increases. For the nanorod, two separate plasmon modes are observed. One at around $525\,\mathrm{nm}$ corresponding to the transverse resonance and one that is red-shifted and depend on the particle's aspect ratio, which corresponds to the longitudinal oscillation.

Moreover, for all spectra, a slight plateau in the extinction is present at shorter wavelengths. At energies above $2.5\,\mathrm{eV}$ ($\sim 500\,\mathrm{nm}$) the energy of photons are sufficient to excite electrons from the filled bands below the Fermi surface to bands above it. These transitions are interband transitions, and as discussed above lead to increased damping and absorption.

2.3 Photothermal effects

Due to electron-phonon relaxation, the favorable properties of plasmonic particles, such as enhanced absorption and scattering, come at the price of significant heat generation. This will, in turn, lead to heat transfer to the environment, producing a thermal gradient close to the nanoparticle. Such elevated thermal environments can be problematic in applications, i.e. in biological processes and other temperature sensitive studies. Nevertheless, in the field of thermoplasmonics they are instead exploited seeing that the plasmonic particle can also be used as a nanoscopic source of heat [41, 59]. In the specific case of optically trapped nanoparticles, and especially nanorods, three photothermal effects stand out as the most important. These are the primary effect of heating, and the two secondary effects of reshaping and bubble formation. Below, we introduce these three effects and discuss possible implications and uses of them.

2.3.1 Heating

The plasmonic resonance is in principle an oscillatory electric current in the metal, and due to ohmic losses, heat is generated via energy dissipation. The heat power density at any point in the nanoparticle is therefore related to the value of the electric field in that point. However, owing to the considerably high thermal conductivity of gold, the temperature distribution within a nanoparticle can, for our purposes, be considered as uniform. If such a particle is placed in water, the thermal distribution around it is predominately determined by conductive heat transfer and the thermal conductivity of the water around it. For a sphere in a homogeneous medium under constant illumination, the temperature distribution as a function of radial distance r to the sphere's center can be obtained by solving the steady-state heat equation in spherical coordinates as [41]

$$T(r) = \frac{\Delta T r_0}{r} + T_{\mathrm{amb}}. \tag{2.10}$$

Here, r_0 is the radius of the sphere, and $\Delta T = \frac{\sigma_{\mathrm{abs}} I}{4\pi K r_0}$. I is the intensity of the incoming light and K is the thermal conductivity of the environment.

If the particle of interest has a more intricate shape, or if the geometry is not as easily parameterized (e.g. at an interface), more rigorous analysis or even numerical simulations are needed. However, in Paper I, both analytical calculations according to Eq. (2.10) as well as finite elements simulations (COMSOL) were performed to study nanoparticle temperature distributions around a trapped nanoparticle, and it turned out that Eq. (2.10) is a valid approximation also for low aspect ratio nanorods.

Optical heating of metallic nanoparticles is the most ubiquitous photothermally induced phenomenon in thermoplasmonics. A range of high impact applications based on the effect has been suggested and are currently being studied, including photothermal imaging [42], plasmonic photothermal therapy (PPTT) [43], and heat-assisted magnetic recording [60]. Moreover, trapping based studies have paved the way for applications using heating effects of optically confined particles to enhance chemical reactions [32], in delivery applications [61], and molecular transition studies [62], as well as others [26–30].

2.3.2 Reshaping

Bulk gold is thermally stabile up to its melting point of 1064°C. However, the surface atoms of metallic nanoparticles are known to be substantially more mobile than their bulk counterparts [63] and this mobility is accelerated by a heated environment. For all metallic nanostructures, this property leads to continuous reorganization of the lattice atoms. Particularly for nanorods, the reorganization is found to be driven by a curvature induced diffusion process where adatoms migrate from high to low curvature areas [64], resulting in a rod becoming shorter and wider, eventually forming the thermodynamically stable sphere.

Rigorous studies of the reshaping of predominately immobilized gold nanorods have been conducted especially focusing on pulsed laser illumination [65–68]. A few particularly noteworthy examples of applications of pulsed laser reshaping are dense data storage [7], production of ultra-narrow dispersions in colloidal ensembles of nanorods [69], and controlled termination of heating during PPTT to prevent harming healthy cells [70].

Under continuous wave (CW) illumination, nanoparticles tend to be even more prone to reshaping. In a pioneering work by Petrova *et al.* on photothermally induced reshaping [71], the thermal stability of nanorods under pulsed and continuous wave illumination was compared. They found that significantly different temperatures were needed to reshape the nanorods in the two cases. For pulsed laser illuminated nanorods, reshaping set in at around 700°C, whereas under continuous wave illumination the rods were seen to reshape at as low temperatures as 150°C. This indicates that heating duration rather than instantaneous temperature governs the surface driven diffusion process since the short laser pulses do not provide sufficient time at elevated temperature for atomic reorganization.

Further fundamental studies of reshaping due to CW laser illumination have been quite sparse since this reshaping is solely a thermal effect. Hence, much of the understanding of reshaping under CW illumination can be taken from the field of thermal reshaping, where the environment is homogeneously heated [72, 73]. Therefore, reshaping of optically trapped gold nanorods is a known problem; however, any rigorous study of photothermally induced reshaping during optical trapping is lacking and the effect has only been mentioned in passing (e.g. in the supporting information of reference [25]).

The issue with poor thermal stability of metallic nanoparticles, and rods in particular, can be somewhat mended by capping the particle in a shell of dielectric material [74]. This could be a valid approach in applications where the advantageous near-field enhancement of the plasmonic structures is not of interest since the surface of the nanoparticle is rendered inaccessible. In relation to optically trapped nanoparticles, no such investigation has been undertaken yet, since the near-field are generally of interest. Therefore, in Paper I we instead set out to characterize the reshaping. However, for future applications the increased thermal stability that a dielectric shell offers could be beneficial.

2.3.3 Bubble formation

Water can be superheated to above the ordinary boiling point ($100°$C) at ambient pressure, and even above this temperature there is an energy barrier separating the two phases (liquid and gas). The reason why boiling macroscopically usually occurs at $100°$C is because of nucleation sites, such as scratches or dust particles on the container surface, where sufficient amounts of molecules in gas state can gather to form bubbles. Hence, if protrusions or contaminations are small or lacking, superheated temperatures can be reached. Photothermal heating of metallic nanoparticles can routinely generate temperatures of above $100°$C, and in a water environment superheating to more than $200°$C has been observed. This and the fact that if the temperature increases further, bubble formation occurs around the nanoparticle is discussed in references [75–77]. Initial studies of nanobubbles around metal nanoparticles were performed for pulsed laser illumination [78–81]. Continuous wave excitation for bubble generation has been studied both on ensemble level [75, 82, 83] and single particle level [84, 85], and it turns out that even for reasonably low power densities (1- 50 mW/μm^2) bubble formation can occur.

One important concept related to bubble formation is that of Laplace pressure. This is the pressure difference at any curved interface between a gas and a liquid. It arises from the minimization of surface energy at the interface and is related to the surface tension of the liquid, Γ. For a spherical bubble it can be written as follows [86]:

$$\Delta P = \frac{2\Gamma}{R}, \tag{2.11}$$

where R is the bubble radius. From this, one understands that a smaller bubble implies a higher pressure difference. Several works have used the concept of Laplace pressure balanced with the vapor pressure of the steam inside the bubble to analyze the temperature threshold for bubble formation and the size of the bubble [77, 78, 84, 85]. We found this analysis useful in some interpretations made from data in Paper I. However, it should be noted that some critique has been raised towards this interpretation [41, 79].

Chapter 3

Optical tweezers

Just as in the case of plasmonics, the field of optical tweezers has matured over several decades. While there is certainly a range of interesting fundamental studies left to undertake regarding optically induced forces, optical tweezers systems are routinely used as an important tool for manipulating small objects in labs and at companies all over the world. The following chapter aims to introduce the aspects essential for the thesis, so for a comprehensive review of the system, see the excellent book by Jones *et al.* [87] or reviews on the topic [13, 88].

3.1 Optical forces

Optical tweezers work on an elegantly simple principle: Interacting photons will transfer some or all their momentum to an object via elastic or inelastic collisions, and hence exert a force on it. The light thus subjects the particle to a force, which can be decomposed into a scattering force component (F_{scat}) and a gradient force (F_{grad}) component. The scattering force is a non-conservative force acting in the propagation direction of the light. It arises from scattering and absorption processes and is hence proportional to the intensity of light. The gradient force arises from the fact that light polarizes the particle, which in turn experiences a force. This force is conservative and will direct a particle in the gradient of the electromagnetic field. The gradient force is therefore responsible for the confinement in optical tweezers. Three-dimensional confinement will be obtained when the gradient force overcomes the scattering force. In order to achieve strong gradient forces experimentally, microscope objectives with high numerical aperture[1] are employed due to their large deflection angles.

It is generally difficult to confine metallic nanoparticles in three dimensions with optical tweezers. This is due to their strongly enhanced scattering and absorption close to the LSPR, which makes the scattering force component larger than the gradient force. However, if one detunes the trapping laser from the LSP resonance wavelength for small metallic nanoparticles, 3D confinement is possible [19]. At the same time, the

[1]Numerical aperture is a dimensionless quantity which describes how large the collection cone of a lens or objective is. NA = $n_{\text{m}} \sin\theta$ where n_{m} is the refractive index of the surrounding medium and θ is the largest angle that the objective can collect light from.

resonance effects can be beneficial for some applications. In those cases, one can sacrifice one dimension of manipulation for stable confinement in two dimensions by using alternative configurations for optical tweezers. Such include counterpropagating optical traps [11, 89], and the surface repulsion technique employed in the experiments performed in this thesis. In this approach, the destabilizing scattering force is counteracted by Coulomb repulsion from an interface with the same charge polarity as the nanoparticle. The underlying physics of this is discussed in Section 3.3.

For a particle with arbitrary size and shape, the force acting on the particle from the optical tweezers can be calculated by integrating Maxwell's stress tensor over a closed surface containing the particle [3]. One then requires values for the electromagnetic field in every point on that surface. This can be obtained analytically from Mie calculations for spherical particles, or by using the numerical methods mentioned in Section 2.2.1 for more complex shapes and geometries. Also here, the quasi-static approximation can be employed to estimate optical forces on small spherical and spheroidal particles. As derived by Ashkin and Gordon in 1983 [90], the induced dipole is acted on by a Lorentz force, and when the dipole moment $\mathbf{p}$ and the incoming electric field $\mathbf{E}$ are linearly related (as in Eq. (2.4)) the total force can be decomposed into gradient and scattering force components, as

$$\mathbf{F}_{\text{grad}} = \frac{\varepsilon_0 \varepsilon_{\text{m}}}{4} \nabla \left(\mathbf{E}^* \cdot \boldsymbol{\alpha}' \cdot \mathbf{E} \right) \tag{3.1}$$

$$\mathbf{F}_{\text{scat}} = \frac{\varepsilon_0 \varepsilon_{\text{m}}}{2} \text{Im}\{\mathbf{E}^* \cdot \boldsymbol{\alpha}'' \cdot \nabla \mathbf{E}\}, \tag{3.2}$$

where * denotes the complex conjugate. For particles with a scalar polarizability (i.e. spheres, or nanorods aligned with the Cartesian axes of the incoming light) and by introducing $I = |\mathbf{E}|^2$, the expressions can be simplified further to

$$\mathbf{F}_{\text{grad}} = \frac{\varepsilon_0 \varepsilon_{\text{m}}}{4} \alpha' \nabla I, \qquad \mathbf{F}_{\text{scat}} = \frac{\varepsilon_0 \varepsilon_{\text{m}}}{2} \alpha'' \text{Im}\{\mathbf{E}^* \cdot \nabla \mathbf{E})\}.$$

If the electromagnetic field of a Gaussian beam is expressed using the paraxial approximation[2], the optical forces on particles fulfilling the quasi-static approximation can now be calculated (derivations outlined in reference [92]). Figure 3.1 displays results of such calculations performed for a nanorod of length 80 nm and width 40 nm (see extinction spectra in Figure 2.3), as it is placed in the focus of a Gaussian beam with divergence equal to that of an objective with numerical aperture NA = 1.4. To illustrate the importance of the LSP resonance on the trapping stability, the forces are visualized for two trapping wavelengths: one at 660 nm laser light (red light, Figure 3.1a) and one at 1064 nm (NIR light, Figure 3.1b). For the red laser, the scattering component dominates, and the particle is propelled in the propagation direction of the light. The NIR laser excites the particle far away from resonance and produces an optical force that is dominated by the gradient force, and hence confines the particle in 3D.

[2]The validity of the paraxial model is decreasing as the angle of incoming radiation increases. Hence, for high NA objectives, the estimated forces will differ from their true

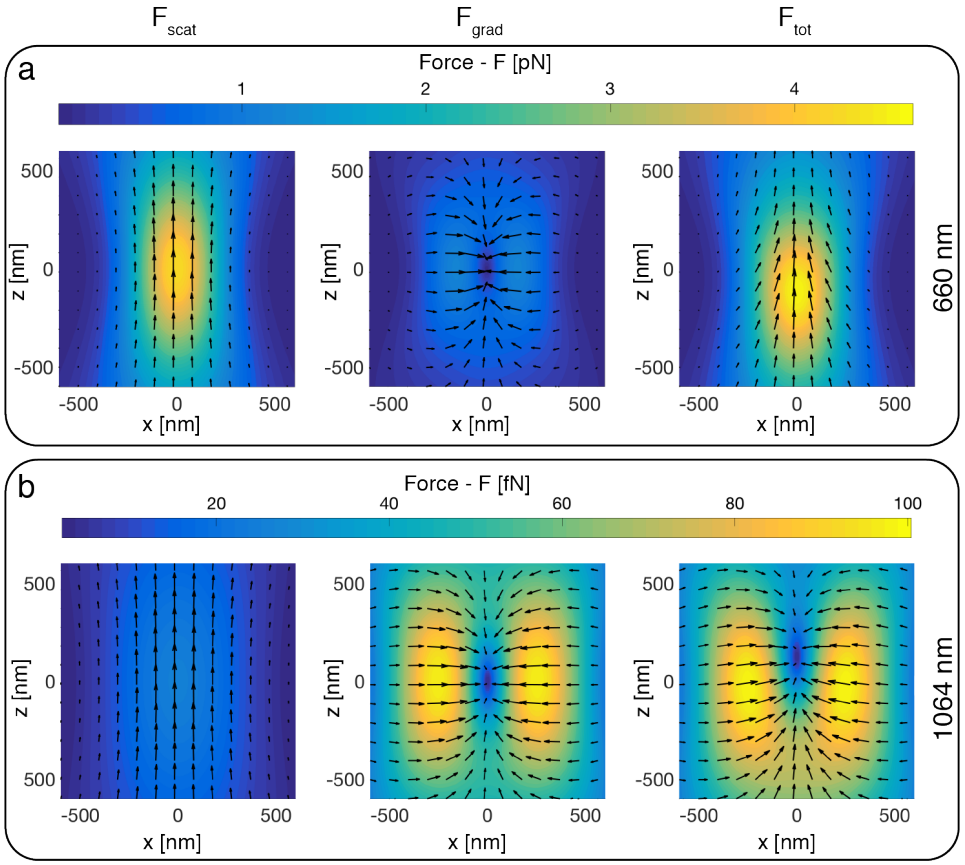

FIGURE 3.1: Optical forces for a prolate spheroid gold nanoparticle (80 nm long and 40 nm wide) with a longitudinal LSP resonance at around 610 nm, in diffraction limited laser tweezers with circularly polarized laser light at the wavelength of (a) 660 nm, and (b) 1064 nm. The light is focused through an objective of NA = 1.4 and has a power of 8 mW. The leftmost graphs show the scattering component, the middle ones the gradient force component, and the rightmost the total force.

As seen from Eq. (3.1), a particle of positive polarizability (refractive index higher than its surrounding) will be directed towards the high-intensity region of the light, whereas one of negative polarizability will be expelled from the trap. For plasmonic particles, the sign of the real part of the polarizability may change when crossing the LSPR resonance due to a phase change of the resonance. This will lead to the gradient force being attractive for light on the low-frequency (red) side of the LSPR peak, whereas it is repulsive for high-frequency (blue) light [24].

3.2 Brownian motion

Even if optical tweezers allow nanoparticles to be confined to impressively small volumes, their motion cannot be stopped completely. The erratic and seemingly random motion of small particles has been observed and pondered over for centuries. An early documented discussion about such motion and its underlying cause is found in the Roman philosopher

values [91]. Nevertheless, since the purpose here is to illustrate the qualitative properties of the Gaussian optical trap, such deviations are overlooked.

Lucretius's "Of the Nature of Things" [93] where he eloquently describes it as

> "Observe what happens when sunbeams are admitted into a building and shed light on its shadowy places. You will see a multitude of tiny particles mingling in a multitude of ways... their dancing is an actual indication of underlying movements of matter that are hidden from our sight... It originates with the atoms which move of themselves. Then those small compound bodies that are least removed from the impetus of the atoms are set in motion by the impact of their invisible blows and in turn cannon against slightly larger bodies. So the movement mounts up from the atoms and gradually emerges to the level of our senses, so that those bodies are in motion that we see in sunbeams, moved by blows that remain invisible."

Indeed, such random motion referred to as Brownian motion is caused by collisions between the particle and its surrounding molecules, as proven by Einstein in 1905 [94]. It turns out that the motion of the Brownian particle is well described by complementing Newton's equation of motion with a stochastic term. One obtains the Langevin equation of motion for *translational* Brownian motion as,

$$m\ddot{\mathbf{r}}(t) = -\gamma_{\mathrm{t}}\dot{\mathbf{r}}(t) + \chi(t), \tag{3.3}$$

where $\chi(t)$ is a random force with zero time average and that is uncorrelated in time (i.e. $\langle\chi(t)\rangle = 0$ and $\langle\chi(t)\chi(t')\rangle = 0$). γ_{t} is the particles hydrodynamic friction coefficient for translational motion, which for a sphere in the low Reynolds number regime[3] can be written using Stokes's law as $\gamma_{\mathrm{t}} = 6\pi\eta r_0$. Here, η is the environment's viscosity, which for water can be approximated in an Arrhenius-type equation [39, 96].

In the presence of an external force $F(\mathbf{r})$ (e.g. the optical forces from the laser tweezers) and in the low Reynolds number regime, the Langevin equation can be rewritten as [87]

$$\dot{\mathbf{r}}(t) = -\frac{1}{\gamma_{\mathrm{t}}}F(\mathbf{r}) + \sqrt{2D_{\mathrm{t}}}W(t). \tag{3.4}$$

Here, $D_{\mathrm{t}} = \frac{k_{\mathrm{B}}T}{\gamma_{\mathrm{t}}}$ is the diffusion coefficient, and $W(t)$ is white noise. The acceleration term in Eq. (3.3) is removed since inertial effects are neglected in the low Reynolds number regime.

In the same way as molecular collisions give rise to translational Brownian motion, they can also give rise to *rotational* Brownian motion. This expresses itself as a stochastic torque that causes the particle to randomly change its orientation. Such a process becomes increasingly important for anisotropic particles. The Langevin equation for rotational Brownian motion, including

[3] The Reynolds number characterizes the ratio between inertial and viscous forces on an object in a fluid. Nanoparticles are generally in the "low Reynolds number regime", where viscosity dominates over inertia. In such a regime, the motion of an object is determined by only its momentary force, without any "memory". Reference [95] introduces the topic in a very accessible way.

an externally applied torque $M_{\text{ext}}(\mathbf{r})$ reads [87]

$$\dot{\varphi}(t) = -\frac{1}{\gamma_{\text{r}}} M_{\text{ext}}(\mathbf{r}) + \sqrt{2D_{\text{r}}} W(t). \tag{3.5}$$

Here, $\varphi(t)$ is the rotation angle, whereas γ_{r} is the friction coefficient for rotational motion, and $D_{\text{r}} = \frac{k_{\text{B}}T}{\gamma_{\text{r}}}$ is the diffusion coefficient for rotational motion. Optically induced external torques and rotary motion will be introduced in detail in Chapter 4.

3.2.1 Trapping stiffness

The translational Brownian motion of a particle inside the optical tweezers gives rise to positional oscillations. For small fluctuations, the force acting on an optically trapped particle is approximately linear. The strength of the restoring force acting on the particle in one dimension can, therefore, be described as a Hookean spring with spring constant k, i.e. its stiffness. Characterizing the trapping stability of the optical tweezers (referred to as trap stiffness) is both an established method for calibrating and quality-testing optical tweezers, and for measuring valuable parameters such as force, viscosity, and temperature.

In the one-dimensional case of Eq. (3.4) and in the regime where $F(x) = -kx$, the Fourier transform of the stochastic positional fluctuations of the trapped particle generates a Lorentzian frequency-dependent power spectrum according to

$$P(f) = |\tilde{x}(f)|^2 = \frac{D_{\text{t}}}{2\pi^2} \frac{1}{f_{\text{c}}^2 + f^2}. \tag{3.6}$$

Here, $f_{\text{c}} = \left(\frac{k}{2\pi\gamma_{\text{t}}}\right)$ is defined as the corner frequency of the Lorentzian, containing k as the trapping stiffness of the optical tweezers [97]. Consequently, we can obtain an expression for the trapping stiffness as

$$k = 2\pi\gamma_{\text{t}} f_{\text{c}}. \tag{3.7}$$

By measuring the positional fluctuations of a particle in the trap and Fourier transforming these, the power spectrum can be obtained. The corner frequency can thereafter be extracted by fitting the experimentally obtained power spectrum to Eq. (3.6), and together with an estimate for the friction coefficient, the trap stiffness can be measured.

3.2.2 Hot Brownian motion

So far, the Brownian diffusion considered above has taken place in a homogeneous environment, where the particle is at equilibrium with its surroundings. This implies there are no gradients in any of the surroundings' properties. In Section 2.3 the fact that a plasmonic particle is significantly heated by light was introduced. This heating leads to strong thermal and viscous gradients in the particle's surroundings. This holds true for any optically trapped particle and especially for metallic

nanoparticles, due to ohmic heating. It is not apparent from the homogeneous case how a Brownian particle in these temperature-induced non-equilibrium environments should behave, and another theory that captures this is needed.

Since the time scale for heat conduction is faster than the characteristic diffusion time of the particle, the surrounding's gradient will be comoving with the particle. It turns out that the dynamics of such a particle can be well described by an effective temperature and viscosity in a homogenous medium, which gives the particle the same diffusive behavior as the real heated one in the thermal gradient. This effective temperature and viscosity (giving rise to an effective diffusion coefficient) is discussed for translational motion in references [98, 99], and for rotational motion in [100].

Due to the fact that rotational and translational motion sample their environments differently (expressed as a more localized velocity flow field for rotational motion in reference [100]), the temperatures associated to translation ($T_{\mathrm{HBM,t}}$) and rotation ($T_{\mathrm{HBM,r}}$) will be different. They relate to each other and the nanoparticle surface temperature (T_{surf}) and surrounding (T_0) according to $T_0 \leq T_{\mathrm{HBM,t}} \leq T_{\mathrm{HBM,r}} \leq T_{\mathrm{surf}}$. The relationship between these temperatures has been verified experimentally by several independent experiments [25, 101].

3.3 Surface interactions

In the studies performed for this thesis, stable confinement of metallic nanoparticles is obtained by balancing the destabilizing scattering component of the optical force with a repulsive force from a surface with the same charge polarity as the nanoparticle (Figure 3.2), instead of the attractive gradient force. The particle will, therefore, be trapped approximately in two dimensions "against" the interface. The motion and performance of a metallic nanoparticle trapped in this configuration are influenced by the surface; however, to what extent was unknown at the beginning of this work. For example, the thermal environment is altered by the proximity to a medium of higher thermal conductivity (e.g. glass). Moreover, as a particle performs Brownian motion near an interface, the drag that it experiences increases as it gets closer to the surface. The drag coefficients are different for different degrees of freedom (i.e. translation or rotation, parallel or perpendicular to the surface) and each can be approximated using Faxén's laws [102, 103].

In aqueous solutions, the interaction and forces between charged surfaces, such as the particle and the interface, are described by the DLVO theory (see Section 3.3.1 below). In Paper III, we discuss a force model, based on DLVO theory, that predicts the behavior of the nanoparticle, and analyze how the vicinity to the interface affects the optically trapped nanoparticle.

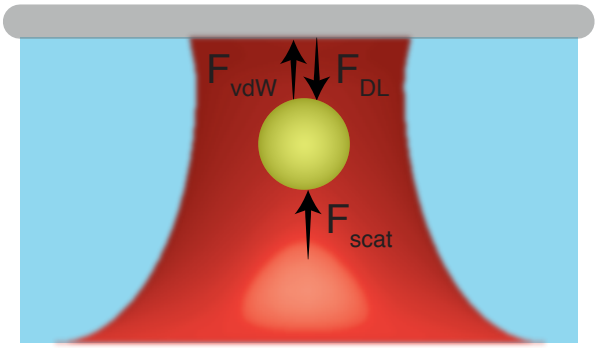

FIGURE 3.2: Decomposition of forces involved in the confinement in the laser's propagation direction when trapping metallic nanoparticles against an interface of same charge polarity as the nanoparticle. Coulomb repulsion (F_{DLR}, double layer repulsion) is counteracting the scattering force (F_{scat}). The short-range van der Waals force (F_{vdW}) also comes into play as the particle approaches the surface.

3.3.1 DLVO theory

The interaction between a nanoparticle and a surface in an aqueous environment stems from the interaction between charges in the objects as well as ionic layers at their surfaces. This results in a force that can be decomposed into two components; the van der Waals force (vdW) and the Coulomb force (double layer repulsion, DL). The following paragraphs introduce the origin of the two forces in line with the comprehensive book by Israelachvili [104], whereas the equations relevant for the work in the thesis are outlined in Paper III.

The van der Waals force results from correlation between instantaneous multipolar (primarily dipolar) fluctuations of adjacent objects. For two single atoms or molecules, such interactions include only the two entities' multipoles. However, going to nanoparticles and even macroscopic bodies the interaction between all component multipoles needs to be summed to provide a measure of the force. Therefore, the vdW force is highly dependent on the shape of the interacting objects.

A surface in a liquid can become charged either by ionization of its surface atoms or by adsorption of ions from solution. This surface charge will attract oppositely charged counter-ions, some of which will bind to the surface in a so-called Stern (or Helmholtz) layer, whereas others form a diffuse electric double layer as an atmosphere around the particle. Such charged counter-ion clouds are responsible for the repulsive force between objects in solution. Relevant measures for the strength and range of these repulsive forces are captured in the zeta potential and the Debye length. These describe the potential difference between the edge of the stabile counter-ion cloud and the surrounding medium, and the thickness of the double layer, respectively. Double layer forces can be derived from the Poisson-Boltzmann equation, and our special case of a spherical particle near an interface is approximately obtained through the Derjaguin approximation, both of which are outlined in detail in reference [104].

Chapter 4

Optically induced rotation

Conventional optical tweezers allow confinement and manipulation of particles thanks to the fact that light can impart momentum on matter. It turns out that light can also transfer *angular momentum* to an object, as verified experimentally as early as 1936, when Beth demonstrated a macroscopically detectable angular displacement of a birefringent waveplate as circularly polarized light was passed through it [33][1].

The fundamental observations of light-induced torques in the early 20th century did not amount to much follow-up work at the time. However, the interest was rekindled as optical tweezers grew more common, and it turned out that forces and torques could be applied simultaneously for full control of a small, immobilized object.

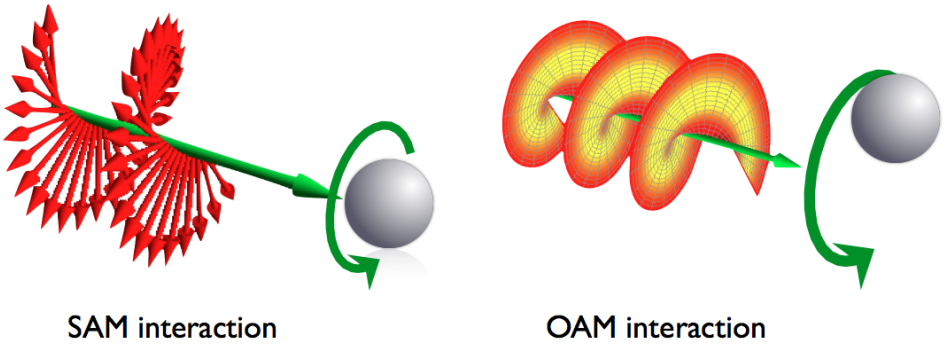

FIGURE 4.1: Illustration of the function and difference between a light beam carrying spin angular momentum (SAM, left) through its polarization state, and orbital angular momentum (OAM, right) through its phase front.

Angular momentum can be carried by light in two different forms, either by its polarization or the shape of its wavefront. These two types are referred to as spin angular momentum (SAM) [33], and orbital angular momentum (OAM) [105], and their function and difference are illustrated in Figure 4.1. Early optical rotation experiments in optical tweezers used both SAM [34, 106] and OAM [107–109] to drive rotation. Generally, the torque induced

[1] It is interesting to note that, when a birefringent crystal changes the polarization state of light, through conservation of angular momentum the crystal must be subjected to torque as well. Therefore what Beth saw, is what happens for all waveplates changing the polarization state of light, if the waveplate is free to rotate. If not, the torque is transferred via the holder to Earth.

by SAM will drive the object to spin around its own axis, whereas OAM-transfer induces a motion around the optical axis (Figure 4.1). In the work performed in this thesis, transfer of SAM is used to cause an optical torque.

Apart from experimental geometries where light itself carries angular momentum, objects in optical tweezers can experience a torque also from other effects. These include alignment with the linear polarization direction of light for anisotropic particles [110, 111], using cleverly designed micromachines to re-direct linear momentum to angular momentum (often referred to as the windmill effect) [112–116], and dynamic positional control of multiple traps inducing a torque [117], to name a few.

The majority of studies on optically induced torques have been concerned with microscopic objects [118–123]. However, as with optical tweezers, it was after a while recognized that the advantageous properties of plasmonic nanoparticles could be useful for enhanced optical torques as well as forces [37, 38]. The optical torque, exerted via SAM on metallic nanostructures, can originate from either absorption or scattering of photons, depending on the geometry of the particle. Rotation of a small, spherically symmetric particle, will be solely due to absorption. However, for other shapes with different rotational symmetry, e.g. a nanorod, the induced torque will originate mainly from scattering [124]. Through these interactions, gold nanoparticles have been made to spin in water with impressively high rotation frequencies above several kHz for nanospheres [39] and several tens of kHz for nanorods [40], creating a high-speed rotary nanomotor system.

This chapter will outline the fundamental physical considerations for driving nanoparticles to rotate with light using the rotary nanomotor platform discussed in references [39] and [40]. Thereafter, some other techniques for driving rotation of metallic nanoparticles are reviewed.

4.1 Optical torque and rotation of nanoparticles

In the rotation geometry of concern to these studies, the nanoparticle is trapped against a cover glass, and rotation will be induced around the optical axis of the incoming laser light. For rotation around one axis, the equation of motion can be written as

$$J\ddot{\varphi}(t) = M_{\text{opt}} + M_{\text{f}} + M_{\text{s}}, \tag{4.1}$$

where J is the moment of inertia for the particle, φ is the orientation angle, M_{opt} is the driving optical torque, M_{f} the opposing frictional torque from the surrounding liquid, and M_{s} a stochastic torque due to rotational Brownian motion.

The frictional torque from the surrounding liquid is counteracting the optical torque. For a small spherical or spheroidal particle, the flow of liquid around the object is laminar due to the low Reynolds number. Consequently, the friction torque can be expressed as $M_{\text{f}} = -\pi\eta(T)L^3\Omega g$ [40], where L is the length of the particle, $\eta(T)$ is the viscosity of the

surrounding water, and Ω is the instantaneous angular velocity of rotation. g is a geometrical shape correction factor, that for spheres is equal to one, and for spheroidal particles is written as [125]

$$g = \frac{-e^3}{-2\xi_0 + (\xi_0^2+1)\hat{\xi_0}} \cdot \left[2\xi_0(\xi_0^2-1)\tanh^{-1}\left(\frac{1}{\xi_0}\right) + \frac{-4+8\xi_0^2-3\xi_0(\xi_0^2-1)\hat{\xi_0}}{3}\right], \tag{4.2}$$

expressed in terms of the reciprocal eccentricity of a spheroid $\xi_0 = \frac{1}{e} = \frac{1}{\sqrt{1-\left(\frac{b}{a}\right)^2}}$, with semi-major and -minor axis a and b, and $\hat{\xi_0} = \ln\left(\frac{\xi_0+1}{\xi_0-1}\right)$.

The total optical torque is composed of an absorption component (M_{abs}) and a scattering component (M_{scat}) according to $M_{\text{opt}} = M_{\text{abs}} + M_{\text{scat}}$. For circularly polarized light, the absorption torque can be estimated as $M_{\text{abs}} = \frac{\sigma_{\text{abs}} I_{\text{inc}}}{\omega}$ where I_{inc} is the laser tweezer's intensity, and ω is the angular frequency of the trapping laser. The scattering component of the torque is more challenging to calculate analytically. However, from knowing the total and absorption component of the torque, the scattering component can be arrived at from $M_{\text{scat}} = M_{\text{opt}} - M_{\text{abs}}$.

A general expression for the total optical torque (M_{opt}) is attainable analytically for spheres and spheroids, either small enough for the quasi-static model to be valid, or using Mie theory. When these can be used to estimate a dipole strength $\mathbf{p}$ that dominates the multipolar response, the time-averaged optical torque perpendicular to the direction of propagation of the laser light can be related to the incoming electric field $\mathbf{E}$ as

$$M_{\text{opt}} = \langle \mathbf{p} \times \mathbf{E} \rangle. \tag{4.3}$$

In the present case of circularly polarized light $\mathbf{E} = \frac{E_0}{\sqrt{2}}(\hat{x}\cos\omega t + \hat{y}\sin\omega t)$, an isotropic particle will experience a torque as $M_{\text{opt}} = \hat{z}\frac{n_{\text{m}}^2}{2}\text{Im}\{\alpha\}|E_0|^2$ [88]. In more complex cases, M_{opt} can instead be obtained by integrating Maxwell's stress tensor from a numerically obtained electric field distribution [124].

When the optical torque is exactly counteracted by the friction torque, the particle is rotating with a constant rotation frequency. An expression for this frequency can be determined to [40]

$$f_{\text{avg}} = \frac{M_{\text{opt}}}{2\pi\gamma_{\text{r}}}, \tag{4.4}$$

where $\gamma_{\text{r}} = \pi\eta(T)gL^3$ is the rotational friction coefficient for a sphere or prolate spheroidal particle, expressed in terms of the geometrical correction factor g (Eq. (4.2)), the temperature dependent viscosity of water $\eta(T)$, and the length of the nanoparticle L. Since the viscosity of water is reduced as temperature increases, it is realized that the enhanced photothermal interaction of plasmonic particles in fact aid in reaching high rotation frequencies. Moreover, since the motion of the nanoparticle is dictated by a temperature dependent property, the motion becomes a handle to locally probe the temperature [101].

4.2 Other rotation schemes using plasmonic structures

The technique outlined above is the one that has shown the highest rotation frequencies in water. Combined with its ease of operation, it is promising as a rotary nanomotor platform. However, there are a variety of other techniques where it might be appropriate to use plasmonically resonant nanostructures to drive rotation of tiny objects. A few of these are discussed below and summarized graphically in Figure 4.2.

Anisotropic metallic nanostructures tend to align their dipole with the linear polarization direction of the optical tweezers, minimizing the energy. Hence, the most rudimentary approach to rotation is to confine a plasmonic structure in a linearly polarized optical trap and thereafter rotate the plane of polarization by mechanically turning a half-wave plate. This is done for silver nanorods and wires by Tong *et al.* [37] and for gold nanorod aggregates by Jones *et al.* [126].

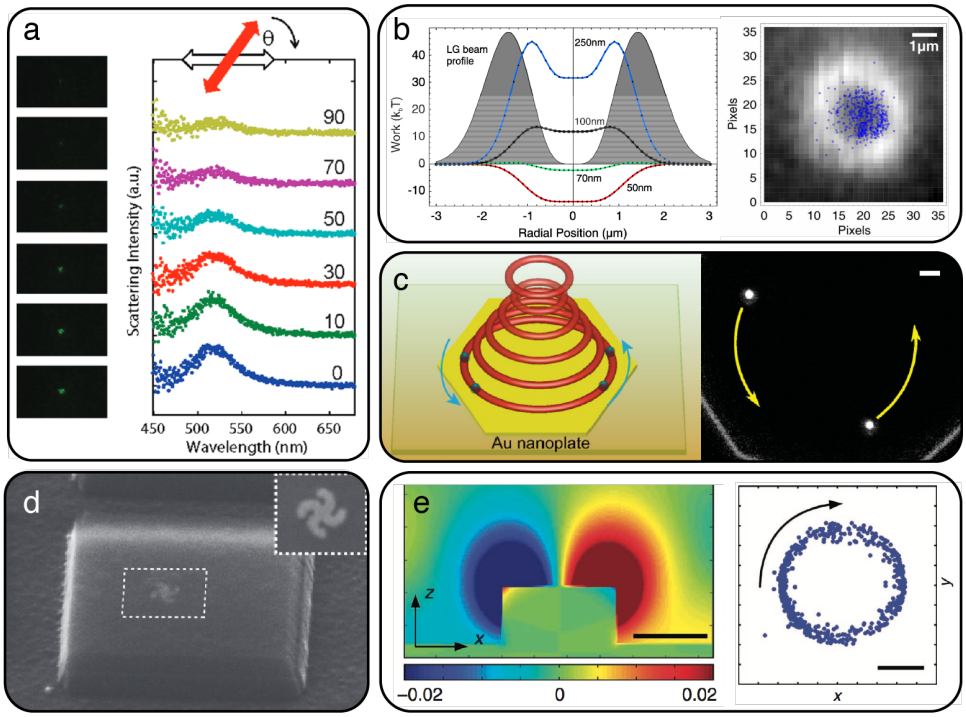

FIGURE 4.2: Alternative ways to drive trapped particles to rotate using light: (a) By aligning anisotropic particle to a linear polarization direction and subsequently rotating that polarization direction with a half wave-plate [37]. (b) Using optical tweezers carrying OAM [127]. (c) In a nodal ring-trap, formed by interfering an OAM beam reflected from a gold mirror with the incoming one [128]. (d) Through engineered nanostructures that scatter linearly polarized light anisotropically and hence experiences a torque [129]. (e) With surface bound plasmonic structures which enhance the electrical near-field and trapping potential [130].

Metallic nanoparticles can also be rotated in focused beams through the transfer of OAM [127, 131]. For example, Dienerowitz *et al.* [127] utilized the repulsive nature of the gradient force on the blue-wavelength side of the plasmon resonance of gold nanospheres to confine them in the low-intensity center of an annular Laguerre-Gaussian beam. Rotation is induced due to the transfer of OAM to the particle, whereas the temperature of the

object is claimed to remain low due to the fact that the particle is confined to the dark region of the beam.

More recently, Figliozzi *et al.* demonstrated a trapping geometry that formed an annulus shaped ring-trap with a diameter of 10μm, where particles are confined and moved around the ring [128]. This is also based on a beam carrying orbital angular momentum; however, using reflection from a single-crystalline gold surface the rotary driving force and confinement could be enhanced.

Exploiting exotically shaped metallic nanostructures, OAM can be imparted to scattered light without the incoming beam carrying it. Through conservation of angular momentum, this will drive a rotation of the object. Liu *et al.* constructed gammadion-shaped gold nanostructures on silica microdisks [129]. Using linearly polarized incident light, they made these structures rotate continuously. Due to the large moment of inertia of the microdisk, the final rotation frequency is low. However, the optical torque stemming from the nanostructure is impressively high and sufficient to rotate the large structure. Therefore, higher rotation frequencies could likely be obtained by reducing the physical size of the hybrid structure.

Alternatively, surface-bound plasmonic structures can be used to generate fields that allow trapping and transfer of angular momentum to confined objects. One such approach is demonstrated by Wang *et al.* [130], where a template-stripped gold nanodisk forms a near-field enhancement which can confine particles below the diffraction limit of far-field radiation. Their geometry also efficiently removes heat, as the plasmonic structure is coupled to a heat sink. Another surface bound technique is presented by Tsai *et al.*, where a plasmonic Archimedes spiral converts a circularly polarized plane wave into a surface plasmon vortex capable of trapping and spinning polystyrene spheres [132].

Chapter 5

Experimental methods

In line with what the philosopher Immanuel Kant stated: ”All knowledge begins with the senses, proceeds then to the understanding...”, experiments provide the physicist access to experiencing a system of interest, in order to form a basis for comprehending it. Therefore, the methods and procedures for making observations in the lab are paramount to reaching new insights. They are presented in the following chapter. The details required to perform the experiments in Paper I are outlined in the method-paper that is Paper II. Hence, those techniques are only summarized below, and the emphasis is rather put on the details needed for Paper III.

5.1 Summary of the appended method-paper

The system for optical trapping of a metallic nanoparticle against a cover glass surface has been used in several publications [39, 40, 101]. Therefore, Paper II (*Construction and Operation of a Light-driven Gold Nanorod Rotary Motor System*) as a method-paper, details the approach for setting up and performing measurements on the rotary nanomotor system. In fact, the main component of this publication is a video-article illustrating the method. The rationale for this form of publication is to reach a broader audience in an accessible format, which hopefully aids the dissemination of the technique. The video is open access and can be reached at the following URL: `https://www.jove.com/video/57947/`.

The first section of the paper outlines the construction of circularly polarized optical tweezers. The system is built around a simple optical trap design where light is collimated, circularly polarized, and directed to a microscope objective. Thereafter, instrumentation for single-photon correlation and dark-field spectroscopy measurements are discussed, where proper alignment procedures and collection is laid out. Hereafter, the experimental procedure for colloid dilution, sample preparation, as well as the collection and analysis of experimental data is presented. The article concludes with some suggestions for solutions to common problems and displays some representative results obtained from the system discussed.

5.2 Total internal reflection microscopy

As a scatterer is placed in an evanescent field, it will convert some of the exponentially decaying near-field radiation into far-field scattered light through a process called frustrated total internal reflection. The intensity of such scattered light depends on where in the decaying evanescent field that the particle is located. By knowing the decay profile of the surface wave, and measuring the scattered intensity, it is possible to extract information about the separation distance between the surface and the scatterer. This is the base of a microscopy technique called *total internal reflection microscopy* (TIRM), which has been successfully used to probe a range of interactions between particles and surfaces [133–141].

In order to reach a measure for the particle-surface separation distance, a translation between scattered intensity and height is needed. Previously, it was recognized that the height-dependent scattering followed the same exponential decay as the evanescent field, $I(h) = I_0 \mathrm{e}^{-\beta h}$. Here, h is the separation distance, I_0 is the scattering intensity at the surface, $\beta = \frac{4\pi}{\lambda}\sqrt{n_{\text{glass}}^2 \sin^2\theta_i - n_{\text{water}}^2}$ is the inverse penetration depth of the evanescent field, expressed in terms of the refractive index of the two media n_{water} and n_{glass}, and the angle of incidence θ_i for the exciting light wave.

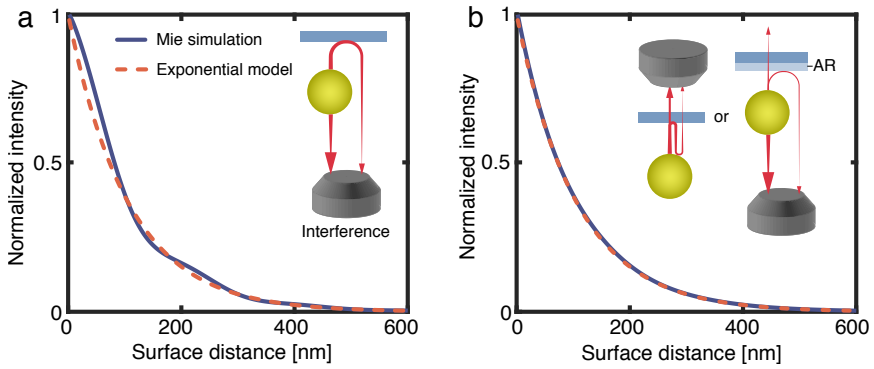

FIGURE 5.1: Scattered TIRM intensity from a 100 nm gold sphere near a glass interface. A Mie-model (blue) is compared to the previously used exponential decay model (dashed orange). (a) For light collected from the water side, the intensity-distance relation is deviating from exponential decay. This trend is explained from interference between directly scattered light with scattered and reflected light (see inset), which becomes negligible if one instead were to collect light from the glass side, or when using an anti-reflection coated surface (as shown in (b)).

In an attempt to verify this exponential dependence, Mie calculations in the vicinity of an interface were performed by PhD student Nils Odebo Länk (For more information, see Paper III). By comparing the intensity-distance translation for collection from the water side of the interface (the present experimental case) from this Mie-model to the exponentially decaying model, a discrepancy manifested as an oscillatory trend is noted (Figure 5.1a). However, when the light is collected on the glass-side of the interface or if an anti-reflection coating is applied at the interface when collecting from the water-side, the oscillation goes away, and the exponential trend is present also for the Mie-model (Figure 5.1b).

Therefore, the discrepancy for the collection geometry at hand is attributed to interference between directly scattered light and light reflected once from the interface. Hence, for the intensity-distance translation performed in Paper III, a table obtained from the Mie simulations is used, rather than the exponential model.

5.3 Brownian dynamics simulations

The Langevin equation for translational motion is written according to Eq. (3.4). This stochastic differential equation needs to be solved to obtain a particle's trajectory. A common way of solving this problem is through iterative methods, where the position at one time step is re-evaluated to the next one by applying a stochastic term to either the position or the velocity of the particle. One particular approach which produces a time efficient solution is by expressing the equation in Liouville operators [142] as done in reference [143]. One time-step in the algorithm is made by the four steps below, and the three-dimensional counterpart is solved by iteratively performing the four steps in each dimension.

Brownian dynamics simulation algorithm:

1. $\tilde{v}_{n+1} = \frac{1}{2}a_n\Delta t + \sqrt{c_0}v_n + v_{\text{th}}\sqrt{1-c_0}W_{1,n}$
2. $x_{n+1} = x_n + \tilde{v}_{n+1}\Delta t$
3. $a_{n+1} = \frac{F_{\text{tot}}(x_{n+1})}{m}$
4. $v_{n+1} = \frac{1}{2}\sqrt{c_0}a_{n+1}\Delta t + \sqrt{c_0}\tilde{v}_{n+1} + v_{\text{th}}\sqrt{1-c_0}W_{2,n}$

Here, $c_0 = \mathrm{e}^{-\gamma_{\text{t}}\Delta t/m}$, $v_{\text{th}} = \sqrt{\frac{k_{\text{B}}T}{m}}$, and $W_{1,n}$ and $W_{2,n}$ are Gaussian random numbers with zero mean, unit variance and that are uncorrelated in time.

A symmetric decomposition of the velocity calculation (Step 1 and 4) is performed in order to reduce the errors involved with the method [143]. When the velocity for the time step is estimated, that velocity is used to calculate the new position (Step 2). The force field that goes into the Brownian dynamics simulation is used to calculate the instantaneous acceleration of the object in each time step of the algorithm (Step 3). The van der Waals and Coulomb force components to this are estimated using models presented in Paper III, and the optical force component is obtained from Mie calculations performed by PhD student Nils Odebo Länk.

As discussed in Section 3.3, the hydrodynamic friction coefficient γ_{t} is for a sphere set by Stokes's law and is governed by the viscosity of the surrounding fluid and the radius of the particle. The value of γ_{t} is affected both by the presence of the surface and the fact that the metallic nanoparticle in the optical trap is performing hot Brownian motion. Therefore, the values going into the simulation routine take these effects into account.

To certify the correctness of the algorithm, the known case of freely diffusing Brownian spheres ($r_0 = 50$ nm) is tested. The external force term is set to zero, and the friction coefficient is made isotropic. The mean square displacement (MSD) in one dimension of such particles' positional fluctuations should be proportional to time [87]. It relates as

$$\mathrm{MSD}_x(t) = \langle (x(t) - x_0)^2 \rangle) \propto t, \tag{5.1}$$

where the brackets denote an ensemble average, $x(t)$ is the particle position at time t, and x_0 is a reference position for each particle. Figure 5.2 displays the MSD in each Cartesian direction for a freely diffusing particle simulated in the model above, and the expected relation is seen to hold. Moreover, the diffusion coefficient of a Brownian particle is related to the mean square displacement as $\mathrm{MSD}(t) = 2D_\mathrm{t}t$. From the data in Figure 5.2, the diffusion coefficient is estimated to 4.5 $\mu\mathrm{m}^2/\mathrm{s}$. This is found to be only 4% away from the analytically derived value for the diffusion coefficient ($D_\mathrm{t} = \frac{k_\mathrm{B}T}{\gamma_\mathrm{t}}$ [87]), and can be compared to the experimentally measured value of around 4 $\mu\mathrm{m}^2/\mathrm{s}$ for the nanoparticles used in Paper III. This agreement is reasonable, considering that experimentally the colloidal nanoparticles suffer from polydispersity and that their hydrodynamic radius is slightly enlarged by the stabilizing double layer.

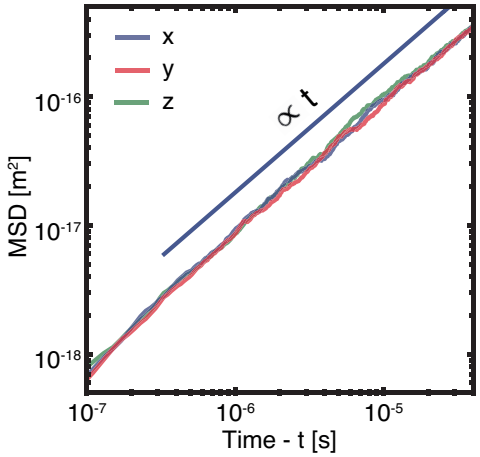

FIGURE 5.2: Mean square displacement of a freely diffusing 100 nm nanosphere. The MSD is proportional to time. From the MSD, the diffusion coefficient of the object can be obtained to 4.5 $\mu\mathrm{m}^2/\mathrm{s}$.

This algorithm is a general one for Brownian motion in several regimes. In our case of low Reynolds number, the inertial term is dropped, causing the mass of the object to no longer matter (Eq. (3.4)). The mass-containing terms in the algorithm could in this limit be rearranged so that the mass cancels out. However, by preserving the mass in the formulas, the physical origin of the terms is more transparent. To verify this, the diffusion coefficient is calculated for a freely diffusing particle of fixed size. When varying the mass over three orders of magnitude, the diffusion coefficient remains at a value of around 4.5 $\mu\mathrm{m}^2/\mathrm{s}$.

5.4 Experimental procedure

A 514 nm laser is free-space coupled via a dove-prism in total internal reflection, to form an evanescent wave for total internal reflection microscopy. The light that is converted from evanescent to far-field scattering by the nanoparticle is collected by an optical fiber and lead to a PMT detector.

The approach to performing the surface probing experiments are to a large extent similar to the ones outlined in the method-paper (Paper II), in terms of particle dilution and experimental procedure. However, the illumination is different, since it is localized at the glass-water interface, and particles only become visible as they diffuse into the evanescent field. Hence, the stage is not translated to locate a suitable particle; rather, the trap is turned on and after some time a particle diffuses into the trap and becomes confined.

To verify the quality of the optical tweezers, a fast camera is used to record as the particle performs translational Brownian motion in the trap. These fluctuations are subsequently transformed into a power spectrum from which the trapping stiffness can be extracted. This is done in accordance with Eq. (3.6) and (3.7).

Ultimately, as a particle is confined, the system allows probing the strength and range of the surface interaction via laser power ramps, or by varying the ionic concentration of the colloid suspension liquid, resulting in variations of the strength of the radiation pressure or Coulomb repulsion forces, respectively. All experiments are performed on at least 20 nanoparticles, in order to reach a statistically significant measurement of the separation distance. Each single nanoparticle experiment is terminated through optical printing [144–146]. Here, the laser power is raised to a level sufficient for radiation pressure to overcome the repulsive Coulomb force, and the particle enters the regime dominated by van der Waals forces. This effectively immobilizes the nanoparticle on the surface, and allows collection of a scattering intensity at a known distance ($\approx$ 0 nm), providing a calibration for a distance measurement in absolute numbers.

Chapter 6

Summary and outlook

Previous chapters in this thesis have introduced the topics essential for the work performed in the appended papers. The two main fundamental fields of plasmonics (Chapter 2) and optical tweezers (Chapter 3) were introduced. It is apparent that there are strong motivations for performing research at the intersection between these two fields, taking advantage both of the strong light-matter interactions and the detailed contact-free manipulation. One such synergetic application is that of rotary nanomotors driven in optical tweezers by a plasmonically enhanced optically induced torque (Chapter 4). Moreover, the experimental approaches required to study such systems were discussed in Chapter 5.

However, up until this point, the information in the thesis has primarily built on work done by others. Now, this chapter instead serves to contextualize and summarize the actual contributions that this thesis makes to move the frontiers of knowledge forward: Contributions which are presented in the appended papers.

6.1 Summary of appended papers

Even though the gold nanorod rotary motor system as presented in reference [40] is comprehensively studied, the thermal effects associated with laser trapping were not addressed. In **Paper I** (*Probing Photothermal Effects on Optically Trapped Gold Nanorods by Simultaneous Plasmon Spectroscopy and Brownian Dynamics Analysis*) a study is presented, where two independent yet complementary measurement techniques are utilized to study such photothermally induced effects on gold nanorods. Through photon correlation spectroscopy and dark-field spectroscopy, it is possible to discern reshaping of a few nanometers during 30-minute experiments, with single-nanorod resolution. Furthermore, from the measurement channels, two gauges for the temperature of the particle's surrounding is attainable, which both show temperatures of superheated liquid water up to 230°C. These measurements are based on the analysis of altered rotational Brownian motion as well as LSP resonance peak shift, caused by the temperature dependent viscosity and refractive index of the surrounding water, respectively.

Up until **Paper III** (*Surface Interactions of Gold Nanoparticles Optically Trapped Against an Interface*), the nanoparticle performance has been

analyzed under the assumption that the separation distance to the surface was large enough for the particle to act as one in a homogenous solution. To certify or falsify this presumption, experiments employing total internal reflection microscopy were carried out. From these, the distance separating a trapped gold nanosphere and the glass interface was measured to be between ∼30-90 nm depending on laser power and double layer force screening. An analytical force model is described, that when inserted as the external force in a Brownian dynamics simulation, closely reproduces the positional fluctuations of the trapped particle. This study is concluded by generalizing the results to include the rotary nanomotors and shows that the temperature of a particle is reduced by less than 10% due to the surface. The translational motion is highly damped by the surface-induced increase in drag, whereas the rotational motion is not affected significantly (<3%).

6.2 Outlook

To some extent, these results conclude a decade worth of fundamental studies on optical trapping of metallic nanoparticles against interfaces performed at the Bionanophotonics division at Chalmers University of Technology[1]. A comfortable degree of understanding of the underlying physics of the platform has been reached. What now remains is to employ the basic insight into nanoparticle tweezing and rotation against interfaces, to reap the possible benefits of the system including localized heating, environmental sensitivity, and impressive torques, for more advanced applications. One such use has already been pursued: The gold nanorod motors have been employed to probe photothermally induced release of DNA from functionalized particles, and detailed estimations of layer thicknesses and conformational changes could be resolved [62].

Potentially the system could be used to probe other exotic forces, such as lateral forces perpendicular to the propagation direction of an incoming beam at the surface [147], or be applied as a tool within nanosurgery as a carrier of active molecules to single cells [61]. Other possible directions that would be interesting to explore is how the rotary performance of the particles could be combined with optical binding forces [148, 149] between multiple particles in a single trap.

Moreover, the knowledge from surface-based trapping can to a certain extent be transferred to methods for stable confinement of nanoparticles in 3D, far from any surface. One such technique capable of 3D trapping of highly absorptive nanoparticles, which is still based on a single laser beam and objective, utilizes a birefringent crystal that splits the trapping laser into two spatially separated foci. These foci can be superimposed, after one has been reflected from a mirror, to form an effectively counter-propagating beam in a single-beam gradient tweezers configuration [150].

[1] These studies were initiated by Tong *et al.* in their 2009 paper on alignment and rotation of plasmonic nanoparticles [37].

With the 2018 Nobel prize being awarded to Arthur Ashkin for the invention of the optical tweezers, the usefulness and value of such techniques are unquestionable. For research, nanoparticle trapping is in many aspects a natural extension to the micron-sized particle trapping systems, with the ability to reach the nanoscale. These systems could be particularly valuable as a testbed for non-equilibrium thermodynamics and when approaching molecular motors. However, commercialization of gold nanoparticle trapping systems has yet to come, mainly due to the complicating amplified Brownian motion.

The findings presented in this thesis can be applied to a wide range of questions. Being able to manipulate nanoscopic objects is a step towards understanding and harnessing the potential involved with matter on this size scale.

Bibliography

1. Collin, S., Etchenique, N. & Moore, T. R. The singing cymbal: Is it really photon momentum? *The Physics Teacher* **54,** 209–211 (2016).
2. Maier, S. A. *Plasmonics: fundamentals and applications* (Springer Science & Business Media, 2007).
3. Novotny, L. & Hecht, B. *Principles of nano-optics* (Cambridge university press, 2012).
4. Anker, J. N. *et al.* Biosensing with plasmonic nanosensors. *Nature Materials* **7,** 442–453 (2008).
5. Huang, X., Jain, P. K., El-Sayed, I. H. & El-Sayed, M. A. Plasmonic photothermal therapy (PPTT) using gold nanoparticles. *Lasers in Medical Science* **23,** 217 (2008).
6. Ghosh, P., Han, G., De, M., Kim, C. K. & Rotello, V. M. Gold nanoparticles in delivery applications. *Advanced Drug Delivery Reviews* **60,** 1307–1315 (2008).
7. Zijlstra, P., Chon, J. W. & Gu, M. Five-dimensional optical recording mediated by surface plasmons in gold nanorods. *Nature* **459,** 410 (2009).
8. Catchpole, K., & Polman, A. Plasmonic solar cells. *Optics Express* **16,** 21793–21800 (2008).
9. Liu, Z., Hou, W., Pavaskar, P., Aykol, M. & Cronin, S. B. Plasmon resonant enhancement of photocatalytic water splitting under visible illumination. *Nano Letters* **11,** 1111–1116 (2011).
10. Aieta, F. *et al.* Aberration-free ultrathin flat lenses and axicons at telecom wavelengths based on plasmonic metasurfaces. *Nano Letters* **12,** 4932–4936 (2012).
11. Ashkin, A. Acceleration and trapping of particles by radiation pressure. *Physical Review Letters* **24,** 156 (1970).
12. Ashkin, A., Dziedzic, J. M., Bjorkholm, J. & Chu, S. Observation of a single-beam gradient force optical trap for dielectric particles. *Optics Letters* **11,** 288–290 (1986).
13. Neuman, K. C. & Block, S. M. Optical trapping. *Review of scientific instruments* **75,** 2787–2809 (2004).
14. Svoboda, K., Schmidt, C. F., Schnapp, B. J. & Block, S. M. Direct observation of kinesin stepping by optical trapping interferometry. *Nature* **365,** 721 (1993).
15. Finer, J. T., Simmons, R. M. & Spudich, J. A. Single myosin molecule mechanics: piconewton forces and nanometre steps. *Nature* **368,** 113 (1994).
16. Abbondanzieri, E. A., Greenleaf, W. J., Shaevitz, J. W., Landick, R. & Block, S. M. Direct observation of base-pair stepping by RNA polymerase. *Nature* **438,** 460 (2005).

17. Raab, E., Prentiss, M, Cable, A., Chu, S. & Pritchard, D. E. Trapping of neutral sodium atoms with radiation pressure. *Physical Review Letters* **59,** 2631 (1987).
18. Chu, S., Bjorkholm, J., Ashkin, A & Cable, A. Experimental observation of optically trapped atoms. *Physical Review Letters* **57,** 314 (1986).
19. Svoboda, K. & Block, S. M. Optical trapping of metallic Rayleigh particles. *Optics Letters* **19,** 930–932 (1994).
20. Hansen, P. M., Bhatia, V. K., Harrit, N. & Oddershede, L. B. Expanding the optical trapping range of gold nanoparticles. *Nano Letters* **5,** 1937–1942 (2005).
21. Selhuber-Unkel, C., Zins, I., Schubert, O., Sonnichsen, C. & Oddershede, L. B. Quantitative optical trapping of single gold nanorods. *Nano Letters* **8,** 2998–3003 (2008).
22. Toussaint, K. *et al.* Plasmon resonance-based optical trapping of single and multiple Au nanoparticles. *Optics Express* **15,** 12017–12029 (2007).
23. Bosanac, L., Aabo, T., Bendix, P. M. & Oddershede, L. B. Efficient optical trapping and visualization of silver nanoparticles. *Nano Letters* **8,** 1486–1491 (2008).
24. Arias-González, J. R. & Nieto-Vesperinas, M. Optical forces on small particles: attractive and repulsive nature and plasmon-resonance conditions. *JOSA A* **20,** 1201–1209 (2003).
25. Ruijgrok, P., Verhart, N., Zijlstra, P, Tchebotareva, A. & Orrit, M. Brownian fluctuations and heating of an optically aligned gold nanorod. *Physical Review Letters* **107,** 037401 (2011).
26. Kyrsting, A., Bendix, P. M., Stamou, D. G. & Oddershede, L. B. Heat profiling of three-dimensionally optically trapped gold nanoparticles using vesicle cargo release. *Nano Letters* **11,** 888–892 (2010).
27. Andres-Arroyo, A., Wang, F., Toe, W. J. & Reece, P. Intrinsic heating in optically trapped Au nanoparticles measured by dark-field spectroscopy. *Biomedical Optics Express* **6,** 3646–3654 (2015).
28. Šiler, M., Ježek, J., Jákl, P., Pilát, Z. & Zemánek, P. Direct measurement of the temperature profile close to an optically trapped absorbing particle. *Optics Letters* **41,** 870–873 (2016).
29. Fedoruk, M., Meixner, M., Carretero-Palacios, S., Lohmüller, T. & Feldmann, J. Nanolithography by plasmonic heating and optical manipulation of gold nanoparticles. *ACS Nano* **7,** 7648–7653 (2013).
30. Bendix, P. M., Reihani, S. N. S. & Oddershede, L. B. Direct measurements of heating by electromagnetically trapped gold nanoparticles on supported lipid bilayers. *ACS Nano* **4,** 2256–2262 (2010).
31. Osinkina, L. *et al.* Tuning DNA binding kinetics in an optical trap by plasmonic nanoparticle heating. *Nano Letters* **13,** 3140–3144 (2013).
32. Ni, W., Ba, H., Lutich, A. A., Jäckel, F. & Feldmann, J. Enhancing single-nanoparticle surface-chemistry by plasmonic overheating in an optical trap. *Nano Letters* **12,** 4647–4650 (2012).
33. Beth, R. A. Mechanical detection and measurement of the angular momentum of light. *Physical Review* **50,** 115 (1936).

34. Friese, M., Nieminen, T., Heckenberg, N. & Rubinsztein-Dunlop, H. Optical alignment and spinning of laser-trapped microscopic particles. *Nature* **394,** 348 (1998).
35. Paterson, L *et al.* Controlled rotation of optically trapped microscopic particles. *Science* **292,** 912–914 (2001).
36. La Porta, A. & Wang, M. D. Optical torque wrench: angular trapping, rotation, and torque detection of quartz microparticles. *Physical Review Letters* **92,** 190801 (2004).
37. Tong, L., Miljkovic, V. D. & Käll, M. Alignment, rotation, and spinning of single plasmonic nanoparticles and nanowires using polarization dependent optical forces. *Nano Letters* **10,** 268–273 (2009).
38. Pelton, M. *et al.* Optical trapping and alignment of single gold nanorods by using plasmon resonances. *Optics Letters* **31,** 2075–2077 (2006).
39. Lehmuskero, A., Ogier, R., Gschneidtner, T., Johansson, P. & Käll, M. Ultrafast spinning of gold nanoparticles in water using circularly polarized light. *Nano Letters* **13,** 3129–3134 (2013).
40. Shao, L., Yang, Z.-J., Andrén, D., Johansson, P. & Käll, M. Gold Nanorod Rotary Motors Driven by Resonant Light Scattering. *ACS Nano* **9,** 12542–12551 (2015).
41. Baffou, G. *Thermoplasmonics: Heating Metal Nanoparticles Using Light* (Cambridge University Press, 2017).
42. Boyer, D., Tamarat, P., Maali, A., Lounis, B. & Orrit, M. Photothermal imaging of nanometer-sized metal particles among scatterers. *Science* **297,** 1160–1163 (2002).
43. Huang, X., El-Sayed, I. H., Qian, W. & El-Sayed, M. A. Cancer cell imaging and photothermal therapy in the near-infrared region by using gold nanorods. *Journal of the American Chemical Society* **128,** 2115–2120 (2006).
44. Boulais, E, Lachaine, R, Hatef, A & Meunier, M. Plasmonics for pulsed-laser cell nanosurgery: Fundamentals and applications. *Journal of Photochemistry and Photobiology C: Photochemistry Reviews* **17,** 26–49 (2013).
45. Chen, H., Shao, L., Li, Q. & Wang, J. Gold nanorods and their plasmonic properties. *Chemical Society Reviews* **42,** 2679–2724 (2013).
46. Willets, K. A. & Van Duyne, R. P. Localized surface plasmon resonance spectroscopy and sensing. *Annu. Rev. Phys. Chem.* **58,** 267–297 (2007).
47. Schuller, J. A. *et al.* Plasmonics for extreme light concentration and manipulation. *Nature Materials* **9,** 193 (2010).
48. Drude, P. Zur elektronentheorie der metalle. *Annalen der Physik* **306,** 566–613 (1900).
49. Yang, H. U. *et al.* Optical dielectric function of silver. *Physical Review B* **91,** 235137 (2015).
50. Gall, D. Electron mean free path in elemental metals. *Journal of Applied Physics* **119,** 085101 (2016).
51. Johnson, P. B. & Christy, R.-W. Optical constants of the noble metals. *Physical Review B* **6,** 4370 (1972).
52. Barnes, W. L., Dereux, A. & Ebbesen, T. W. Surface plasmon subwavelength optics. *Nature* **424,** 824 (2003).

53. Homola, J., Yee, S. S. & Gauglitz, G. Surface plasmon resonance sensors. *Sensors and Actuators B: Chemical* **54,** 3–15 (1999).
54. Meier, M & Wokaun, A. Enhanced fields on large metal particles: dynamic depolarization. *Optics Letters* **8,** 581–583 (1983).
55. Zeman, E. J. & Schatz, G. C. An accurate electromagnetic theory study of surface enhancement factors for silver, gold, copper, lithium, sodium, aluminum, gallium, indium, zinc, and cadmium. *Journal of Physical Chemistry* **91,** 634–643 (1987).
56. Mie, G. Beiträge zur Optik trüber Medien, speziell kolloidaler Metallösungen. *Annalen der physik* **330,** 377–445 (1908).
57. Bohren, C. F. & Huffman, D. R. *Absorption and scattering of light by small particles* (John Wiley & Sons, 2008).
58. Myroshnychenko, V. *et al.* Modelling the optical response of gold nanoparticles. *Chemical Society Reviews* **37,** 1792–1805 (2008).
59. Baffou, G. & Quidant, R. Thermo-plasmonics: using metallic nanostructures as nano-sources of heat. *Laser & Photonics Reviews* **7,** 171–187 (2013).
60. Kryder, M. H. *et al.* Heat assisted magnetic recording. *Proceedings of the IEEE* **96,** 1810–1835 (2008).
61. Li, M., Lohmüller, T. & Feldmann, J. Optical injection of gold nanoparticles into living cells. *Nano Letters* **15,** 770–775 (2014).
62. Šíopová, H., Shao, L., Odebo Länk, N., Andrén, D. & Käll, M. Photothermal DNA release from laser-tweezed individual gold nanomotors driven by photon angular momentum. *ACS Photonics* (2018).
63. Iijima, S. & Ichihashi, T. Structural instability of ultrafine particles of metals. *Physical Review Letters* **56,** 616 (1986).
64. Taylor, A. B., Siddiquee, A. M. & Chon, J. W. Below melting point photothermal reshaping of single gold nanorods driven by surface diffusion. *ACS Nano* **8,** 12071–12079 (2014).
65. Zijlstra, P., Chon, J. W. & Gu, M. White light scattering spectroscopy and electron microscopy of laser induced melting in single gold nanorods. *Physical Chemistry Chemical Physics* **11,** 5915–5921 (2009).
66. Link, S., Burda, C., Nikoobakht, B & El-Sayed, M. A. Laser-induced shape changes of colloidal gold nanorods using femtosecond and nanosecond laser pulses. *The Journal of Physical Chemistry B* **104,** 6152–6163 (2000).
67. Habenicht, A., Olapinski, M., Burmeister, F., Leiderer, P. & Boneberg, J. Jumping nanodroplets. *Science* **309,** 2043–2045 (2005).
68. Gordel, M. *et al.* Post-synthesis reshaping of gold nanorods using a femtosecond laser. *Physical Chemistry Chemical Physics* **16,** 71–78 (2014).
69. González-Rubio, G. *et al.* Femtosecond laser reshaping yields gold nanorods with ultranarrow surface plasmon resonances. *Science* **358,** 640–644 (2017).
70. Takahashi, H., Niidome, T., Nariai, A., Niidome, Y. & Yamada, S. Photothermal reshaping of gold nanorods prevents further cell death. *Nanotechnology* **17,** 4431 (2006).
71. Petrova, H. *et al.* On the temperature stability of gold nanorods: comparison between thermal and ultrafast laser-induced heating. *Physical Chemistry Chemical Physics* **8,** 814–821 (2006).

72. Mohamed, M. B., Ismail, K. Z., Link, S. & El-Sayed, M. A. Thermal reshaping of gold nanorods in micelles. *The Journal of Physical Chemistry B* **102,** 9370–9374 (1998).
73. Liu, Y., Mills, E. N. & Composto, R. J. Tuning optical properties of gold nanorods in polymer films through thermal reshaping. *Journal of Materials Chemistry* **19,** 2704–2709 (2009).
74. Chen, Y.-S. *et al.* Enhanced thermal stability of silica-coated gold nanorods for photoacoustic imaging and image-guided therapy. *Optics Express* **18,** 8867–8878 (2010).
75. Baffou, G., Polleux, J., Rigneault, H. & Monneret, S. Super-heating and micro-bubble generation around plasmonic nanoparticles under cw illumination. *The Journal of Physical Chemistry C* **118,** 4890–4898 (2014).
76. Setoura, K., Werner, D. & Hashimoto, S. Optical scattering spectral thermometry and refractometry of a single gold nanoparticle under CW laser excitation. *The Journal of Physical Chemistry C* **116,** 15458–15466 (2012).
77. Merabia, S., Keblinski, P., Joly, L., Lewis, L. J. & Barrat, J.-L. Critical heat flux around strongly heated nanoparticles. *Physical Review E* **79,** 021404 (2009).
78. Lukianova-Hleb, E. *et al.* Plasmonic nanobubbles as transient vapor nanobubbles generated around plasmonic nanoparticles. *ACS Nano* **4,** 2109–2123 (2010).
79. Metwally, K., Mensah, S. & Baffou, G. Fluence threshold for photothermal bubble generation using plasmonic nanoparticles. *The Journal of Physical Chemistry C* **119,** 28586–28596 (2015).
80. Kotaidis, V, Dahmen, C, Von Plessen, G, Springer, F & Plech, A. Excitation of nanoscale vapor bubbles at the surface of gold nanoparticles in water. *The Journal of Chemical Physics* **124,** 184702 (2006).
81. Lombard, J., Biben, T. & Merabia, S. Kinetics of nanobubble generation around overheated nanoparticles. *Physical Review Letters* **112,** 105701 (2014).
82. Neumann, O. *et al.* Solar vapor generation enabled by nanoparticles. *ACS Nano* **7,** 42–49 (2012).
83. Hühn, D., Govorov, A., Gil, P. R. & Parak, W. J. Photostimulated Au nanoheaters in polymer and biological media: characterization of mechanical destruction and boiling. *Advanced Functional Materials* **22,** 294–303 (2012).
84. Fang, Z. *et al.* Evolution of light-induced vapor generation at a liquid-immersed metallic nanoparticle. *Nano Letters* **13,** 1736–1742 (2013).
85. Hou, L., Yorulmaz, M., Verhart, N. R. & Orrit, M. Explosive formation and dynamics of vapor nanobubbles around a continuously heated gold nanosphere. *New Journal of Physics* **17,** 013050 (2015).
86. De Gennes, P.-G., Brochard-Wyart, F. & Quere, D. Capillarity and Wetting Phenomena: Drops. *Bubbles, Pearls, Waves* **291** (2004).
87. Jones, P. H., Maragò, O. M. & Volpe, G. *Optical tweezers: Principles and applications* (Cambridge University Press, 2015).
88. Lehmuskero, A., Johansson, P., Rubinsztein-Dunlop, H., Tong, L. & Käll, M. Laser Trapping of Colloidal Metal Nanoparticles. *ACS Nano* **9,** 3453–3469 (2015).

89. Tauro, S., Bañas, A., Palima, D. & Glückstad, J. Dynamic axial stabilization of counter-propagating beam-traps with feedback control. *Optics Express* **18,** 18217–18222 (2010).
90. Ashkin, A. & Gordon, J. P. Stability of radiation-pressure particle traps: an optical Earnshaw theorem. *Optics Letters* **8,** 511–513 (1983).
91. Barton, J. & Alexander, D. Fifth-order corrected electromagnetic field components for a fundamental Gaussian beam. *Journal of Applied Physics* **66,** 2800–2802 (1989).
92. Agayan, R. R., Gittes, F., Kopelman, R. & Schmidt, C. F. Optical trapping near resonance absorption. *Applied Optics* **41,** 2318–2327 (2002).
93. Lucretius, T. L. C. *Of the Nature of Things* trans. by Leonard, W. E. (Project Gutenberg, 1997).
94. Einstein, A. Über die von der molekularkinetischen Theorie der Wärme geforderte Bewegung von in ruhenden Flüssigkeiten suspendierten Teilchen. *Annalen der physik* **322,** 549–560 (1905).
95. Purcell, E. M. Life at low Reynolds number. *American Journal of Physics* **45,** 3–11 (1977).
96. Fogel'son, R. & Likhachev, E. Temperature dependence of viscosity. *Technical Physics* **46,** 1056–1059 (2001).
97. Berg-Sørensen, K. & Flyvbjerg, H. Power spectrum analysis for optical tweezers. *Review of Scientific Instruments* **75,** 594–612 (2004).
98. Rings, D., Schachoff, R., Selmke, M., Cichos, F. & Kroy, K. Hot brownian motion. *Physical Review Letters* **105,** 090604 (2010).
99. Falasco, G, Gnann, M., Rings, D & Kroy, K. Effective temperatures of hot Brownian motion. *Physical Review E* **90,** 032131 (2014).
100. Rings, D., Chakraborty, D. & Kroy, K. Rotational hot Brownian motion. *New Journal of Physics* **14,** 053012 (2012).
101. Hajizadeh, F. *et al.* Brownian fluctuations of an optically rotated nanorod. *Optica* **4,** 746–751 (2017).
102. Brenner, H. The slow motion of a sphere through a viscous fluid towards a plane surface. *Chemical Engineering Science* **16,** 242–251 (1961).
103. Leach, J. *et al.* Comparison of Faxén's correction for a microsphere translating or rotating near a surface. *Physical Review E* **79,** 026301 (2009).
104. Israelachvili, J. N. *Intermolecular and surface forces* (Academic press, 2011).
105. Allen, L., Beijersbergen, M. W., Spreeuw, R. & Woerdman, J. Orbital angular momentum of light and the transformation of Laguerre-Gaussian laser modes. *Physical Review A* **45,** 8185 (1992).
106. Ashkin, A. Applications of laser radiation pressure. *Science* **210,** 1081–1088 (1980).
107. He, H, Friese, M., Heckenberg, N. & Rubinsztein-Dunlop, H. Direct observation of transfer of angular momentum to absorptive particles from a laser beam with a phase singularity. *Physical Review Letters* **75,** 826 (1995).
108. Friese, M., Enger, J, Rubinsztein-Dunlop, H & Heckenberg, N. R. Optical angular-momentum transfer to trapped absorbing particles. *Physical Review A* **54,** 1593 (1996).

109. Simpson, N., Dholakia, K, Allen, L & Padgett, M. Mechanical equivalence of spin and orbital angular momentum of light: an optical spanner. *Optics Letters* **22,** 52–54 (1997).
110. Luo, Z.-P., Sun, Y.-L. & An, K.-N. An optical spin micromotor. *Applied Physics Letters* **76,** 1779–1781 (2000).
111. Galajda, P. & Ormos, P. Orientation of flat particles in optical tweezers by linearly polarized light. *Optics Express* **11,** 446–451 (2003).
112. Higurashi, E, Ukita, H, Tanaka, H & Ohguchi, O. Optically induced rotation of anisotropic micro-objects fabricated by surface micromachining. *Applied Physics Letters* **64,** 2209–2210 (1994).
113. Asavei, T., Loke, V. L., Nieminen, T. A., Heckenberg, N. R. & Rubinsztein-Dunlop, H. *Optical paddle-wheel* in *Optical Trapping and Optical Micromanipulation VI* **7400** (2009), 740020.
114. Galajda, P. & Ormos, P. Rotors produced and driven in laser tweezers with reversed direction of rotation. *Applied Physics Letters* **80,** 4653–4655 (2002).
115. Neale, S. L., MacDonald, M. P., Dholakia, K. & Krauss, T. F. All-optical control of microfluidic components using form birefringence. *Nature Materials* **4,** 530 (2005).
116. Lin, X.-F. *et al.* A light-driven turbine-like micro-rotor and study on its light-to-mechanical power conversion efficiency. *Applied Physics Letters* **101,** 113901 (2012).
117. Bingelyte, V, Leach, J, Courtial, J & Padgett, M. Optically controlled three-dimensional rotation of microscopic objects. *Applied Physics Letters* **82,** 829–831 (2003).
118. Friese, M., Rubinsztein-Dunlop, H, Gold, J., Hagberg, P. & Hanstorp, D. Optically driven micromachine elements. *Applied Physics Letters* **78,** 547–549 (2001).
119. Bishop, A. I., Nieminen, T. A., Heckenberg, N. R. & Rubinsztein-Dunlop, H. Optical microrheology using rotating laser-trapped particles. *Physical Review Letters* **92,** 198104 (2004).
120. Leach, J., Mushfique, H., di Leonardo, R., Padgett, M. & Cooper, J. An optically driven pump for microfluidics. *Lab on a Chip* **6,** 735–739 (2006).
121. Arita, Y. *et al.* Rotational dynamics and heating of trapped nanovaterite particles. *ACS Nano* **10,** 11505–11510 (2016).
122. Favre-Bulle, I. A., Stilgoe, A. B., Rubinsztein-Dunlop, H. & Scott, E. K. Optical trapping of otoliths drives vestibular behaviours in larval zebrafish. *Nature Communications* **8,** 630 (2017).
123. Rodríguez-Sevilla, P., Arita, Y., Liu, X., Jaque, D. & Dholakia, K. The temperature of an optically trapped, rotating microparticle. *ACS Photonics* **5,** 3772–3778 (2018).
124. Lee, Y. E., Fung, K. H., Jin, D. & Fang, N. X. Optical torque from enhanced scattering by multipolar plasmonic resonance. *Nanophotonics* **3,** 343–350 (2014).
125. Kong, D., Lin, W., Pan, Y. & Zhang, K. Swimming motion of rod-shaped magnetotactic bacteria: the effects of shape and growing magnetic moment. *Frontiers in Microbiology* **5,** 8 (2014).
126. Jones, P. *et al.* Rotation detection in light-driven nanorotors. *ACS Nano* **3,** 3077–3084 (2009).

127. Dienerowitz, M., Mazilu, M., Reece, P. J., Krauss, T. F. & Dholakia, K. Optical vortex trap for resonant confinement of metal nanoparticles. *Optics Express* **16,** 4991–4999 (2008).
128. Figliozzi, P. *et al.* Driven optical matter: Dynamics of electrodynamically coupled nanoparticles in an optical ring vortex. *Physical Review E* **95,** 022604 (2017).
129. Liu, M., Zentgraf, T., Liu, Y., Bartal, G. & Zhang, X. Light-driven nanoscale plasmonic motors. *Nature Nanotechnology* **5,** 570 (2010).
130. Wang, K., Schonbrun, E., Steinvurzel, P. & Crozier, K. B. Trapping and rotating nanoparticles using a plasmonic nano-tweezer with an integrated heat sink. *Nature Communications* **2,** 469 (2011).
131. Lehmuskero, A., Li, Y., Johansson, P. & Käll, M. Plasmonic particles set into fast orbital motion by an optical vortex beam. *Optics Express* **22,** 4349–4356 (2014).
132. Tsai, W.-Y., Huang, J.-S. & Huang, C.-B. Selective trapping or rotation of isotropic dielectric microparticles by optical near field in a plasmonic archimedes spiral. *Nano Letters* **14,** 547–552 (2014).
133. Prieve, D. C. Measurement of colloidal forces with TIRM. *Advances in Colloid and Interface Science* **82,** 93–125 (1999).
134. Brown, M., Smith, A. & Staples, E. A method using total internal reflection microscopy and radiation pressure to study weak interaction forces of particles near surfaces. *Langmuir* **5,** 1319–1324 (1989).
135. Suresh, L. & Walz, J. Y. Direct measurement of the effect of surface roughness on the colloidal forces between a particle and flat plate. *Journal of colloid and interface science* **196,** 177–190 (1997).
136. Bevan, M. A. & Prieve, D. C. Direct measurement of retarded van der Waals attraction. *Langmuir* **15,** 7925–7936 (1999).
137. Walz, J. Y. & Prieve, D. C. Prediction and measurement of the optical trapping forces on a microscopic dielectric sphere. *Langmuir* **8,** 3073–3082 (1992).
138. Hertlein, C., Helden, L., Gambassi, A., Dietrich, S. & Bechinger, C. Direct measurement of critical Casimir forces. *Nature* **451,** 172 (2008).
139. Helden, L., Eichhorn, R. & Bechinger, C. Direct measurement of thermophoretic forces. *Soft matter* **11,** 2379–2386 (2015).
140. Liu, L., Woolf, A., Rodriguez, A. W. & Capasso, F. Absolute position total internal reflection microscopy with an optical tweezer. *Proceedings of the National Academy of Sciences* **111,** E5609–E5615 (2014).
141. Eichmann, S. L., Anekal, S. G. & Bevan, M. A. Electrostatically confined nanoparticle interactions and dynamics. *Langmuir* **24,** 714–721 (2008).
142. Risken, H. in *The Fokker-Planck Equation* 63–95 (Springer, 1996).
143. Bussi, G. & Parrinello, M. Accurate sampling using Langevin dynamics. *Physical Review E* **75,** 056707 (2007).
144. Urban, A. S., Lutich, A. A., Stefani, F. D. & Feldmann, J. Laser printing single gold nanoparticles. *Nano Letters* **10,** 4794–4798 (2010).
145. Guffey, M. J. & Scherer, N. F. All-optical patterning of Au nanoparticles on surfaces using optical traps. *Nano Letters* **10,** 4302–4308 (2010).

146. Gargiulo, J. *et al.* Accuracy and Mechanistic Details of Optical Printing of Single Au and Ag Nanoparticles. *ACS Nano* **11,** 9678–9688 (2017).
147. Rodríguez-Fortuño, F. J., Engheta, N., Martínez, A. & Zayats, A. V. Lateral forces on circularly polarizable particles near a surface. *Nature Communications* **6,** 8799 (2015).
148. Burns, M. M., Fournier, J.-M. & Golovchenko, J. A. Optical binding. *Physical Review Letters* **63,** 1233 (1989).
149. Miljkovic, V. D., Pakizeh, T., Sepulveda, B., Johansson, P. & Käll, M. Optical forces in plasmonic nanoparticle dimers. *The Journal of Physical Chemistry C* **114,** 7472–7479 (2010).
150. Karpinski, P., Jones, S., Andrén, D. & Käll, M. Counter-Propagating Optical Trapping of Resonant Nanoparticles Using a Uniaxial Crystal. *Laser & Photonics Reviews,* 1800139 (2018).